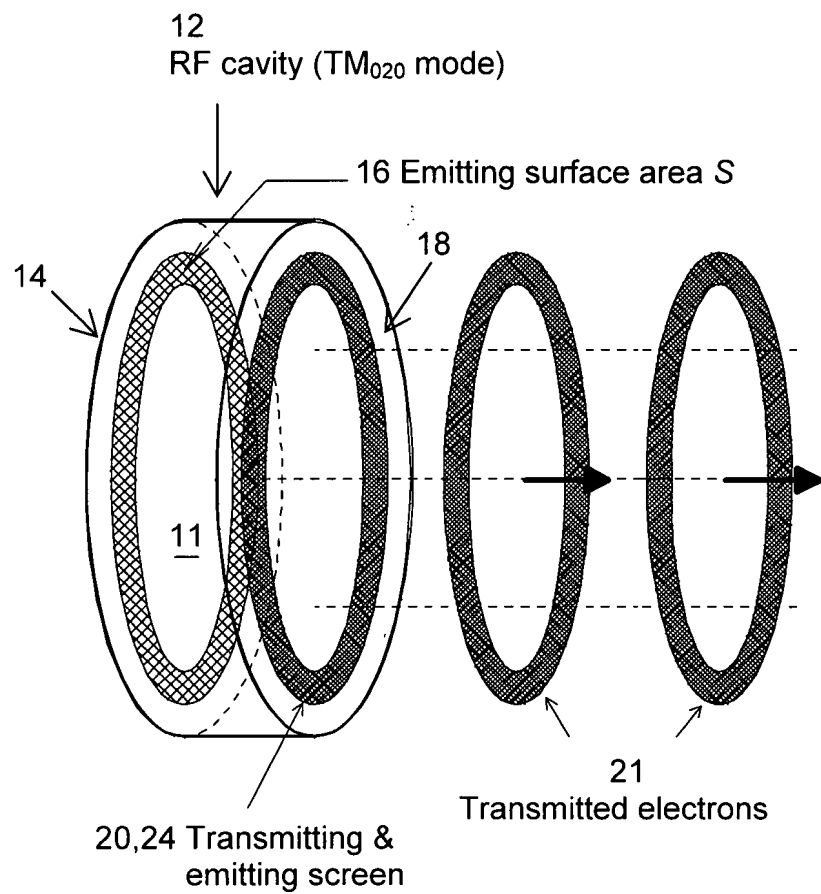




22 Oscillating means 26 Electric field means 10 Electron gun

28 Magnetic field means



11
Electrons between 16 and 20

Figure 1: Perspective view of the micropulse gun for a hollow beam in the TM_{020} mode.
The inner conductor is not shown.

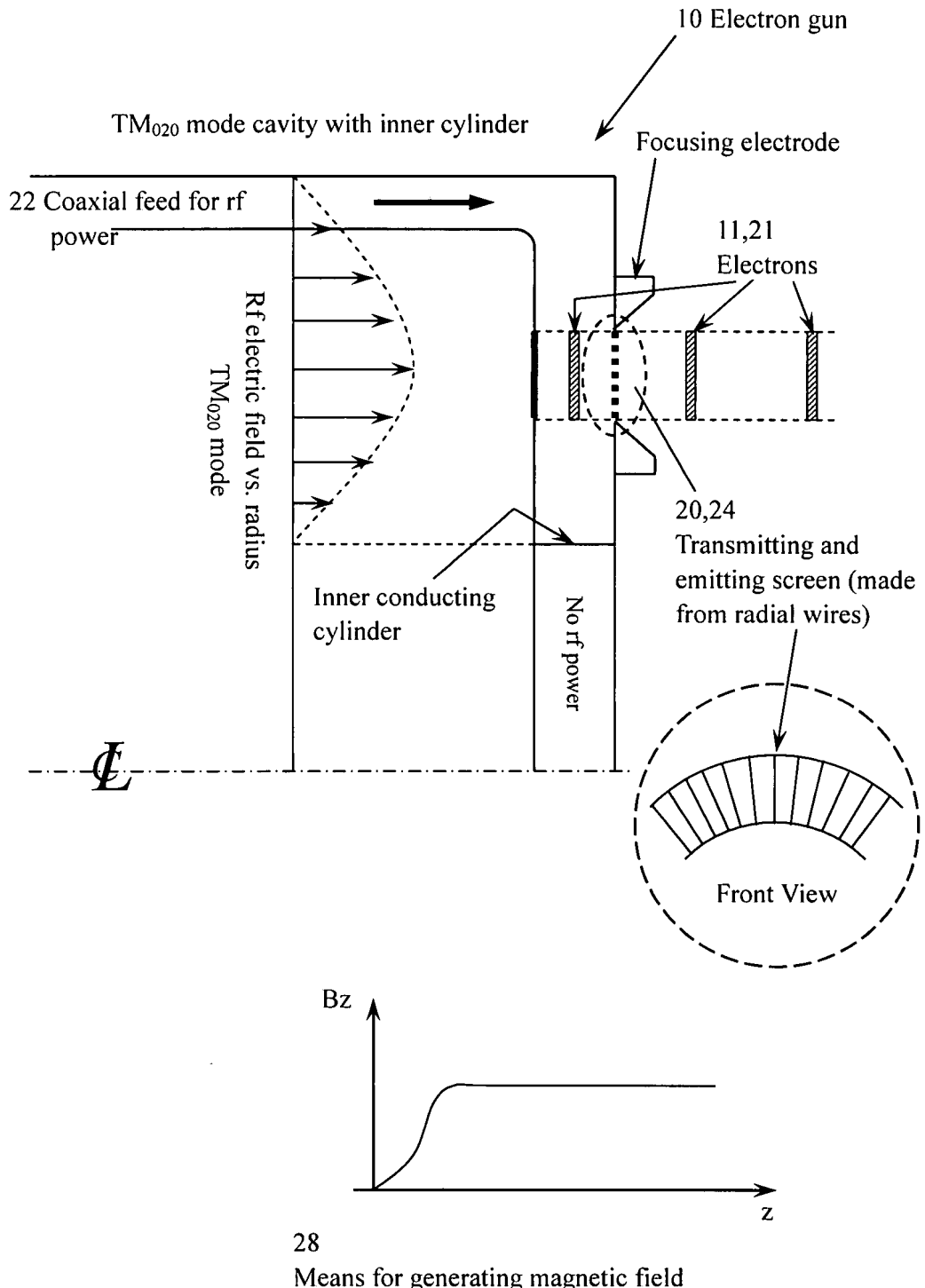


Figure 2: Schematic of rf gun operating in TM_{020} mode.

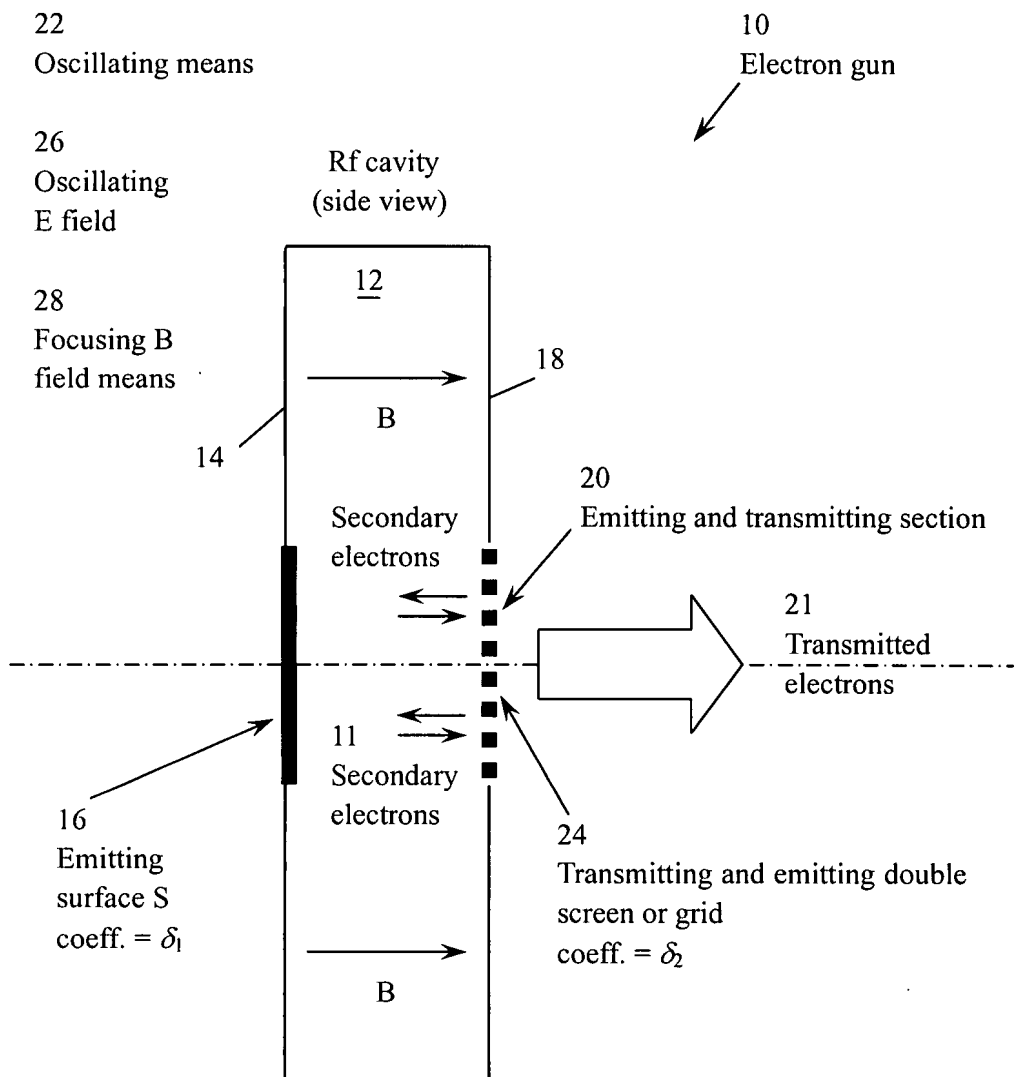
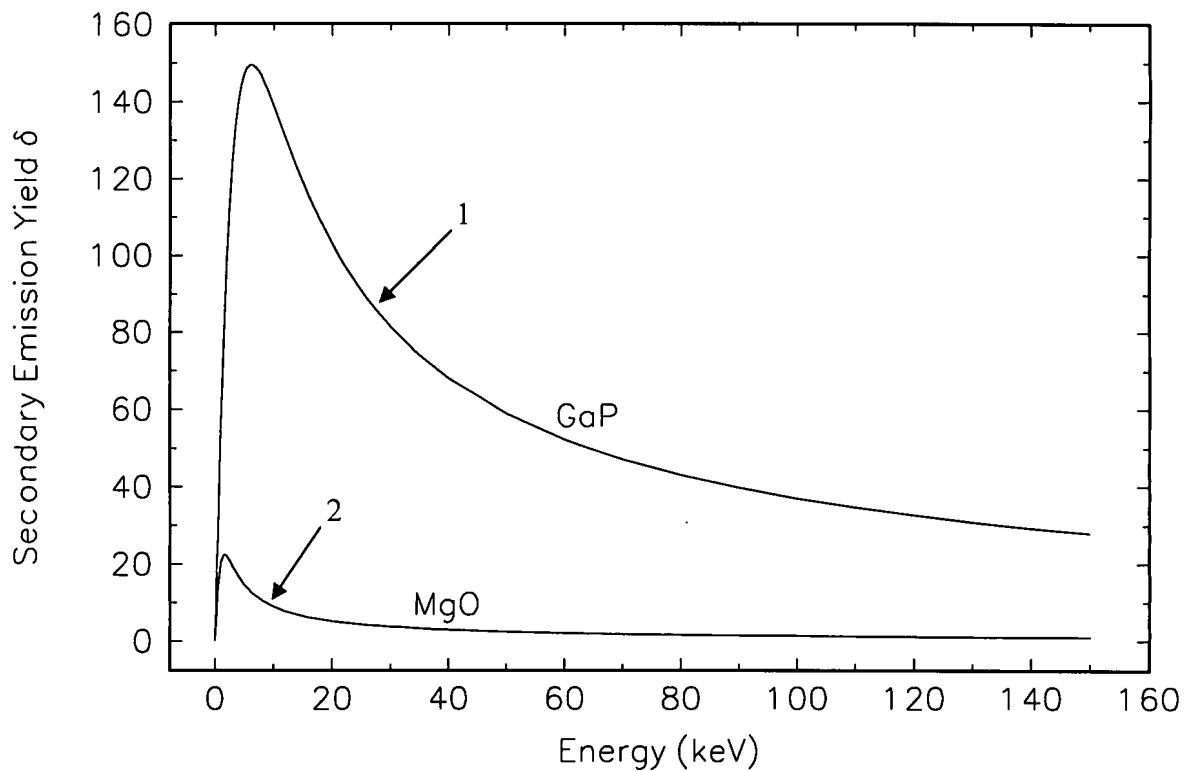
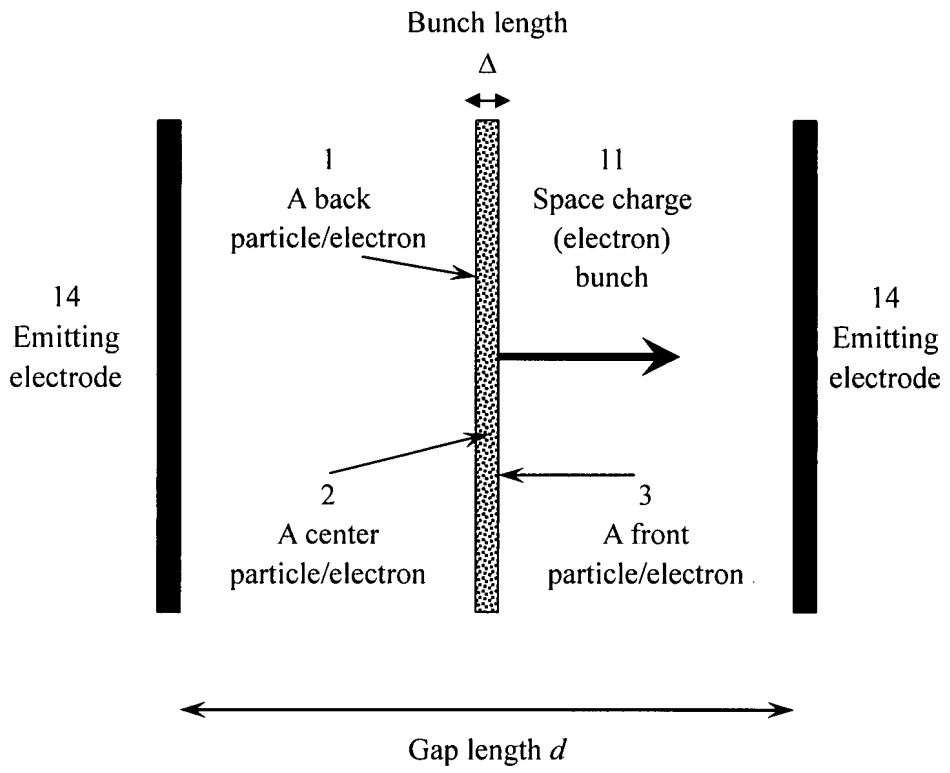


Figure 3: Schematic of micropulse gun for solid beam (TM_{010}) mode. A coaxial feed is used for rf input (not shown).



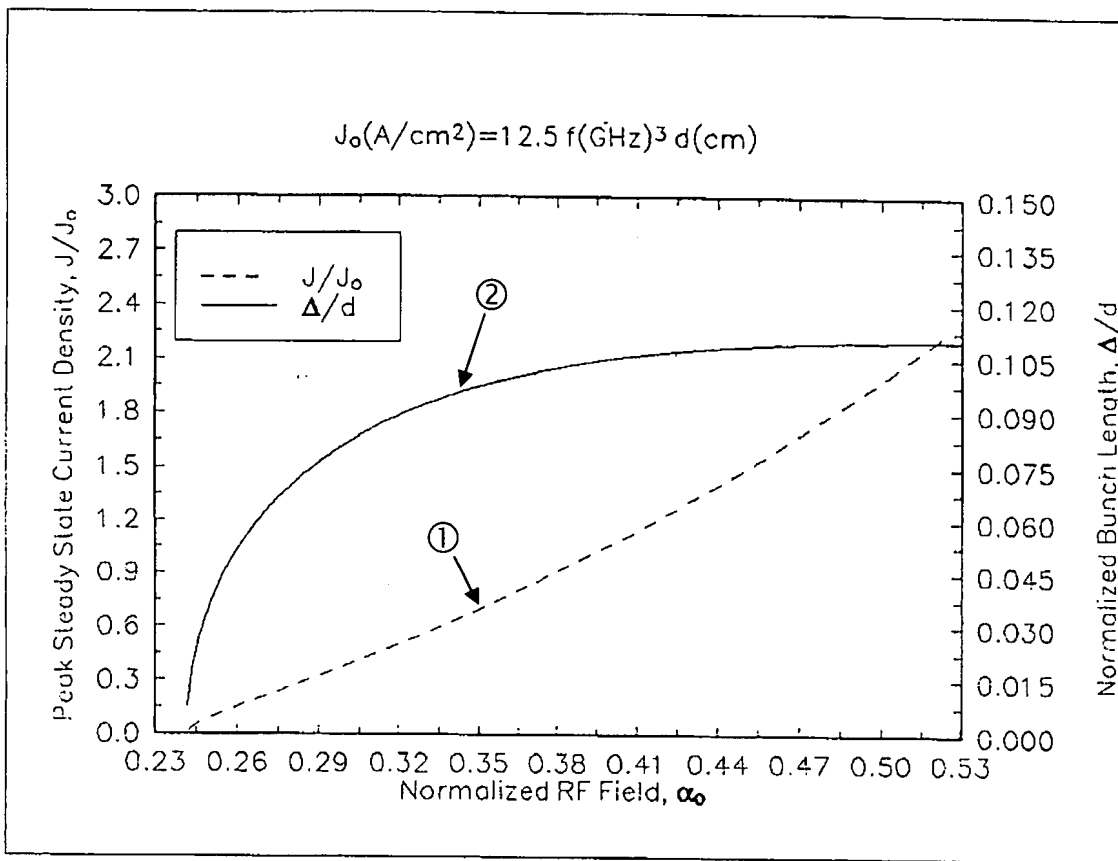
- 1 – Secondary emission yield of GaP
2 – Secondary emission yield of MgO

Figure 4: Secondary electron emission yield curve for GaP and MgO.



- 14 - Emitting electrodes
- 11 - Electron bunch
- 1 - A back particle/electron
- 2 - A center particle/electron
- 3 - A front particle/electron

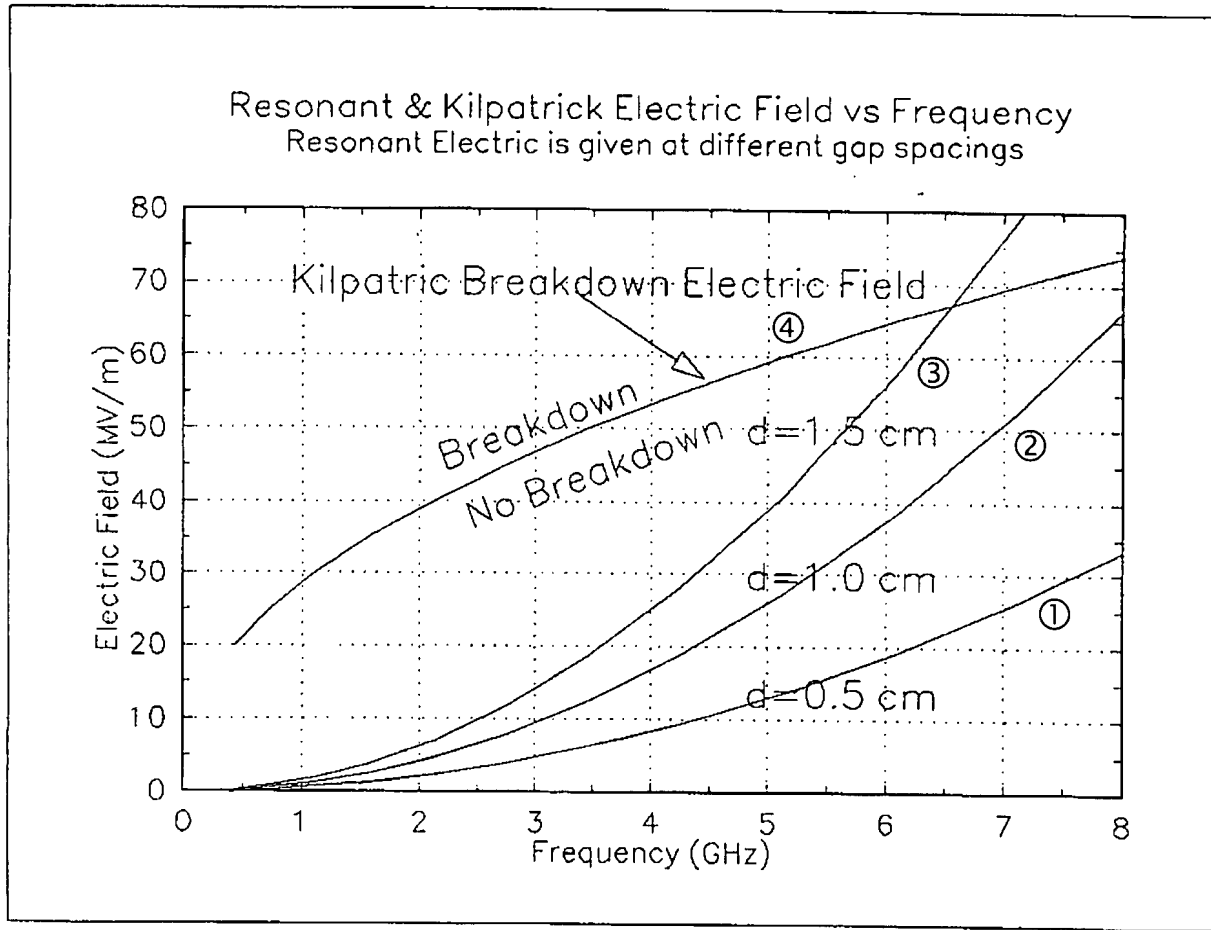
Figure 5. Schematic drawing of model used in theoretical analysis.



① Plot of normalized peak current density at steady state versus rf field.

② Plot of normalized electron bunch length versus rf field.

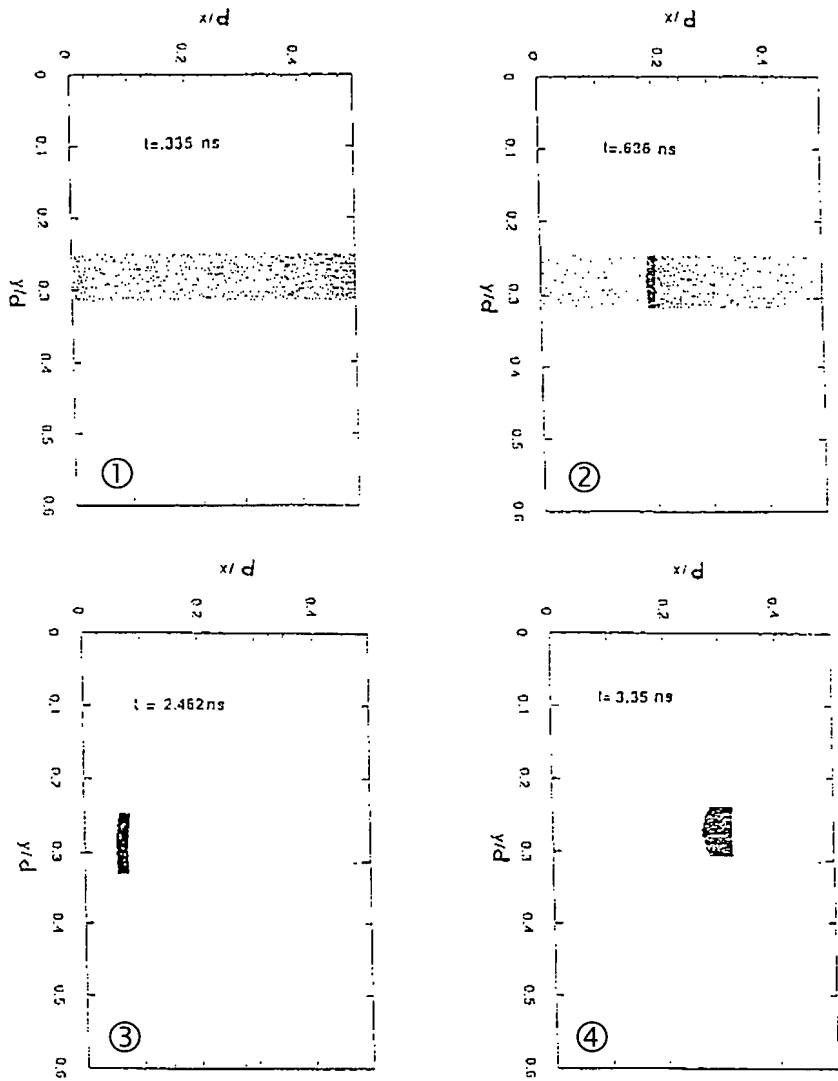
Figure 6: Steady-state current density and bunch length vs. rf field, all parameters are normalized.



- ① Plot of resonant electric field versus frequency for 0.5 cm gap
- ② Plot of resonant electric field versus frequency for 1.0 cm gap
- ③ Plot of resonant electric field versus frequency for 1.5 cm gap
- ④ Plot of Kilpatrick breakdown electric field versus frequency.

Figure 7: Plot of resonant electric fields for $\alpha_0 = 0.453$ and various gap spacings. Also shown is the critical Kilpatrick electric field as a function of rf frequency.

1.3 GHz, xy plot



- ① Plot of electron distribution in the cavity at $t = 0.335 \text{ ns}$.
- ② Plot of electron distribution in the cavity at $t = 0.636 \text{ ns}$.
- ③ Plot of electron distribution in the cavity at $t = 2.462 \text{ ns}$.
- ④ Plot of electron distribution in the cavity at $t = 3.35 \text{ ns}$.

Figure 8: Series of time “snapshots” for a 1.3 GHz, $d = 0.5 \text{ cm}$ cavity using the two-dimensional PIC code with secondary emission. Note the rapid particle build-up and bunching by phase selection. Electrons traverse the horizontal axis. On the vertical axis, emission is limited to the region 0.25 to 0.32 cm.

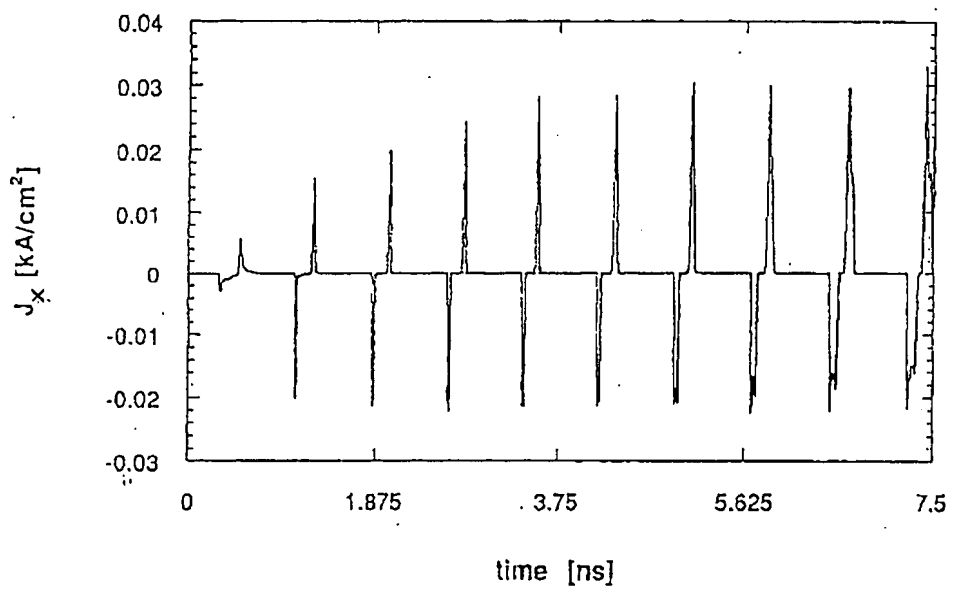


Figure 9: Plot of current density vs. time for simulation with rf frequency 1.3 GHz, voltage amplitude 4.3 kV, $d = 0.5$ cm, and $\alpha_0 = 0.453$.

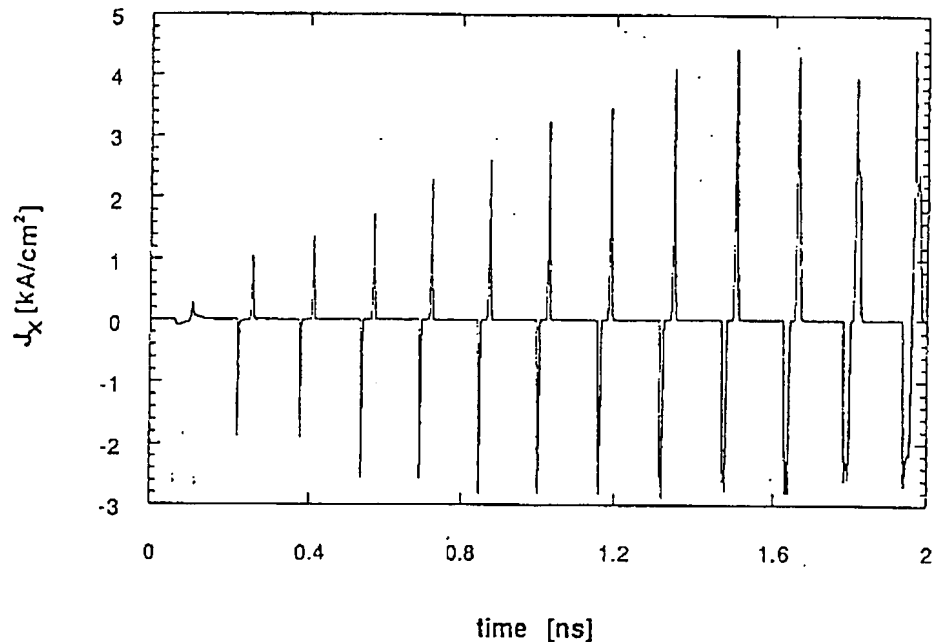


Figure 10: Plot of current density vs. time for simulation with rf frequency 6.4 GHz, voltage amplitude 105 kV, $d = 0.5$ cm, and $\alpha_0 = 0.453$.

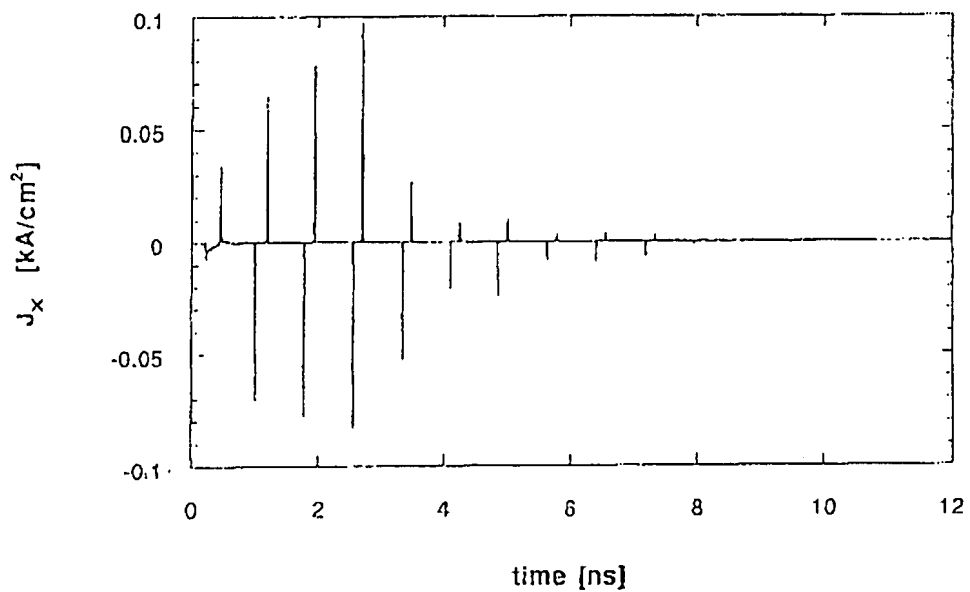


Figure 11: Current density in kA/cm^2 for an off-resonance $d = 0.5 \text{ cm}$ cavity with frequency 1.3 GHz and higher voltage 9.8 kV. Note that not only does current amplification not occur, but the steady-state current is zero.

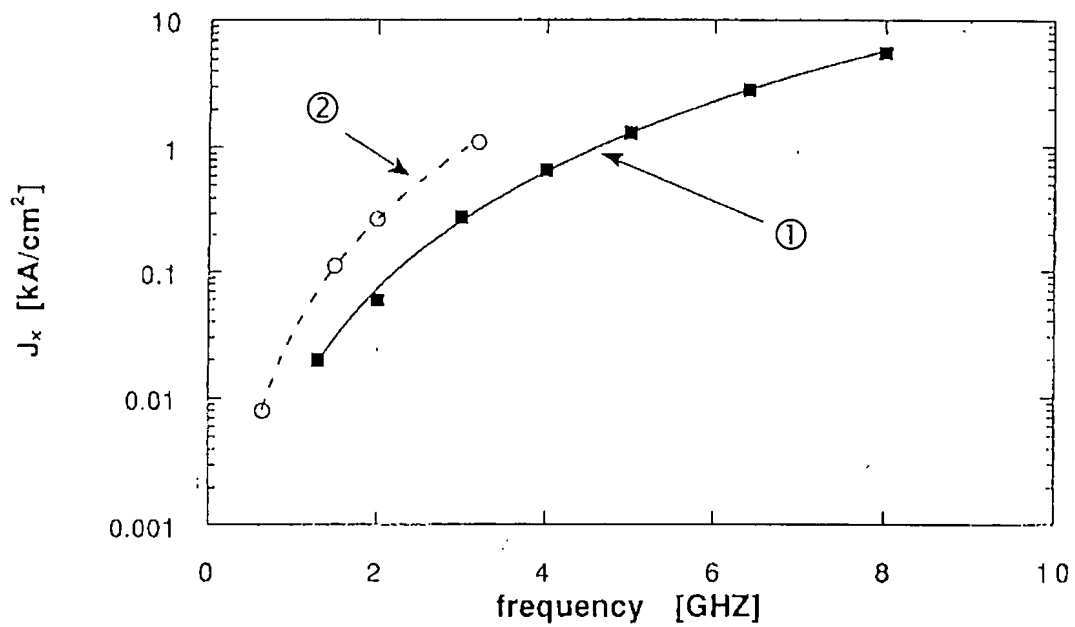
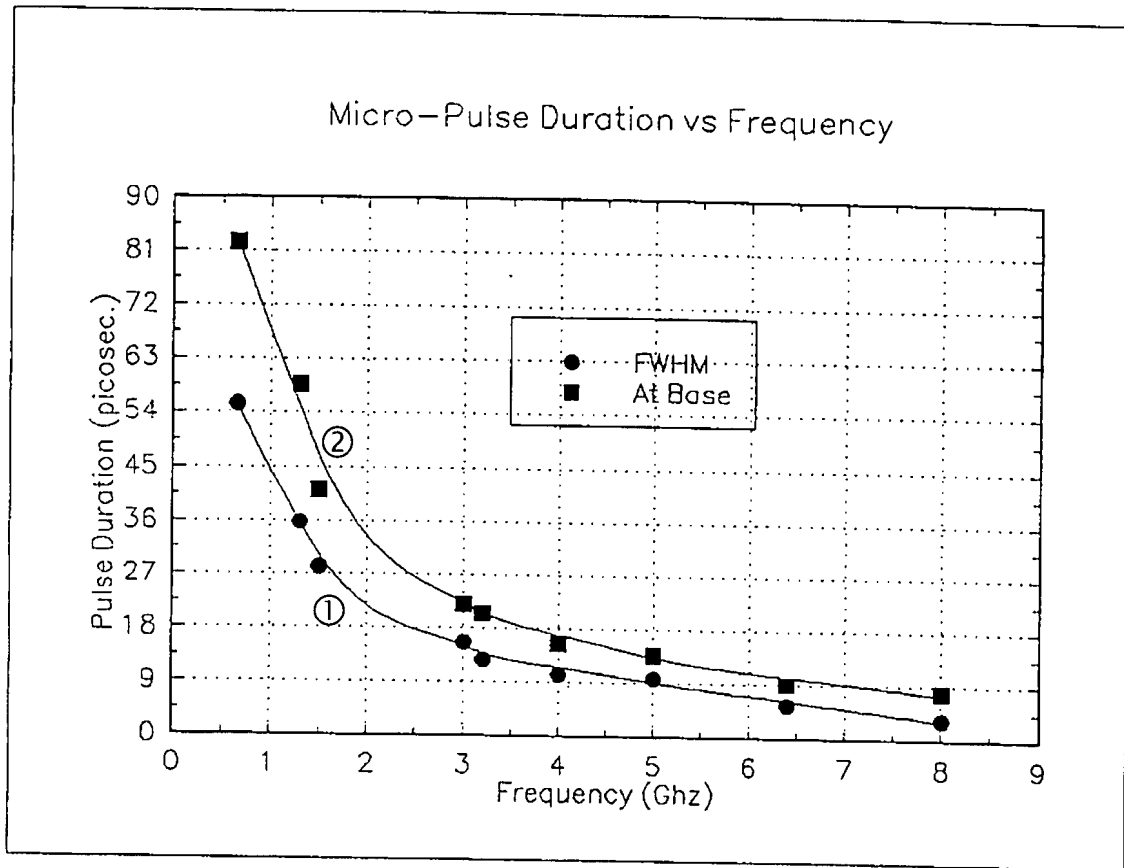
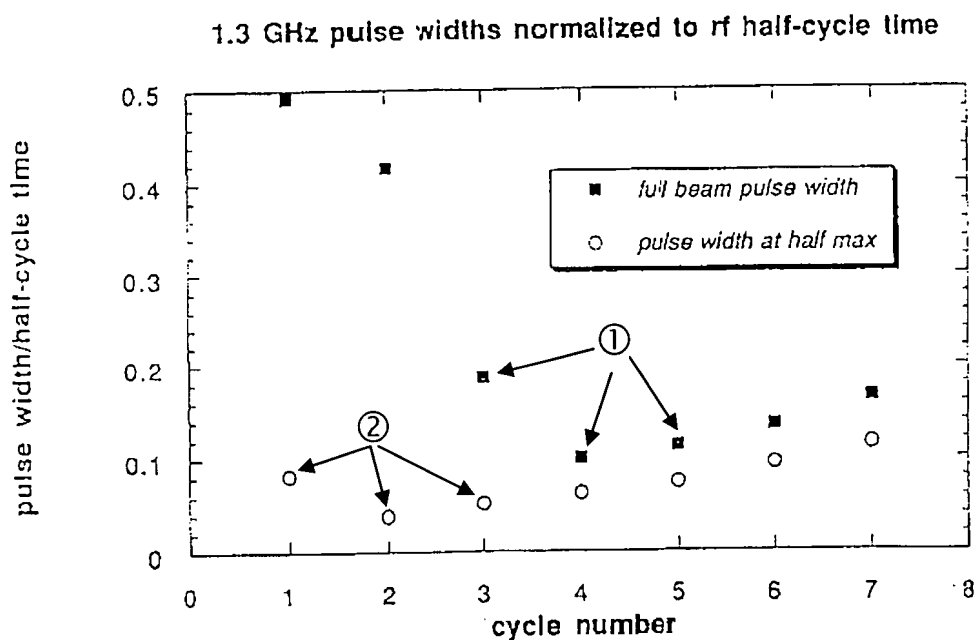


Figure 12: Steady-state current density vs. rf frequency for cavity with $\alpha_0 = 0.453$ and gap lengths of ① 0.5 cm (solid line is a fit using $J_x = 0.008f^{3.15}$) and ② 1.0 cm (dashed line is a fit using $J_x = 0.03f^{3.1}$).



- ① Electron micro-pulse full width at half maximum.
- ② Electron micro-pulse full width at the base of the pulse.

Figure 13: Micro-pulse duration vs. frequency for $\alpha_0 = 0.453$.



- ① (solid square) Beam full width at different rf cycle.
- ② (open circle) Beam full width at half maximum at different rf cycle.

Figure 14: Micro-pulse width (as a fraction of the half-cycle) vs. rf cycle number near the output grid. The full beam pulse width decreases with time, and reaches a minimum at the fourth rf cycle. After saturation there is a slight increase in pulse-width due to space-charge effects.

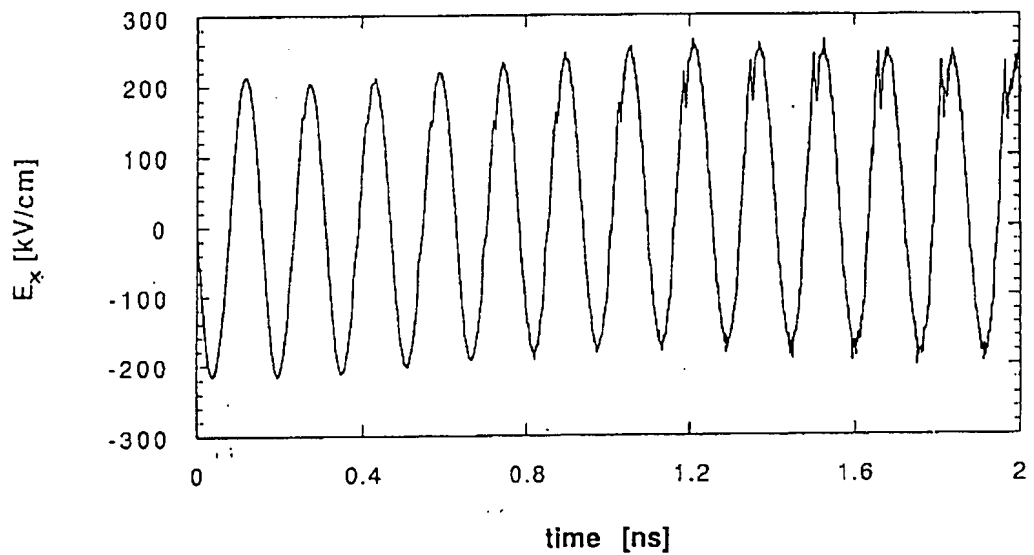


Figure 15: Longitudinal electric field in kv/cm as measured by a probe near the exit grid for the 6.4 GHz, 105 kV simulation.

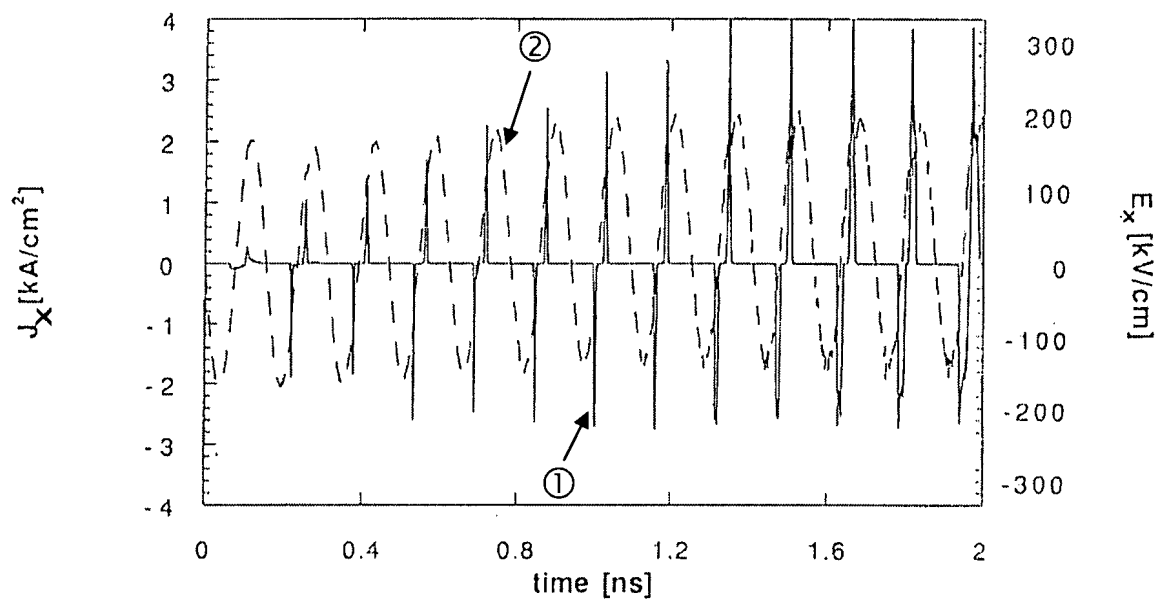


Figure 16: ① Plot of the current density in kA/cm^2 (solid line) and ② the longitudinal electric field (dashed line) for the 6.4 GHz, 105 kV simulation.

Comparison of Theory and Simulation
cavity gap=d = 0.5 cm, J_0 (A/cm²)=12.5 f(GHz)³ d(cm)

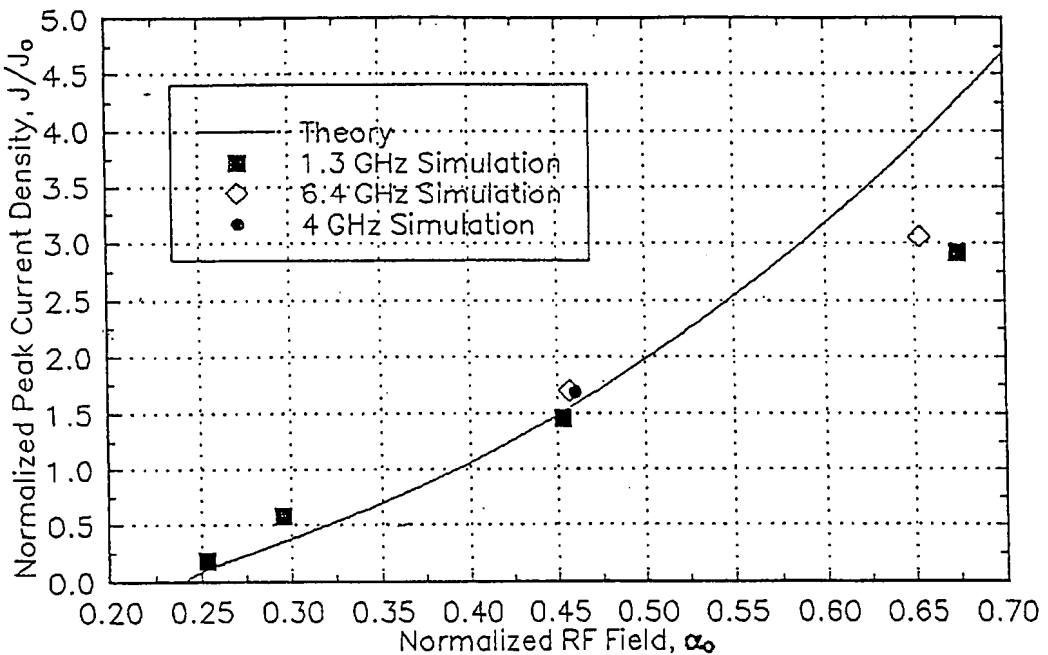


Figure 17: Resonant Tuning Curve (both simulation and theory) showing the tolerance of the micropulse electron gun.

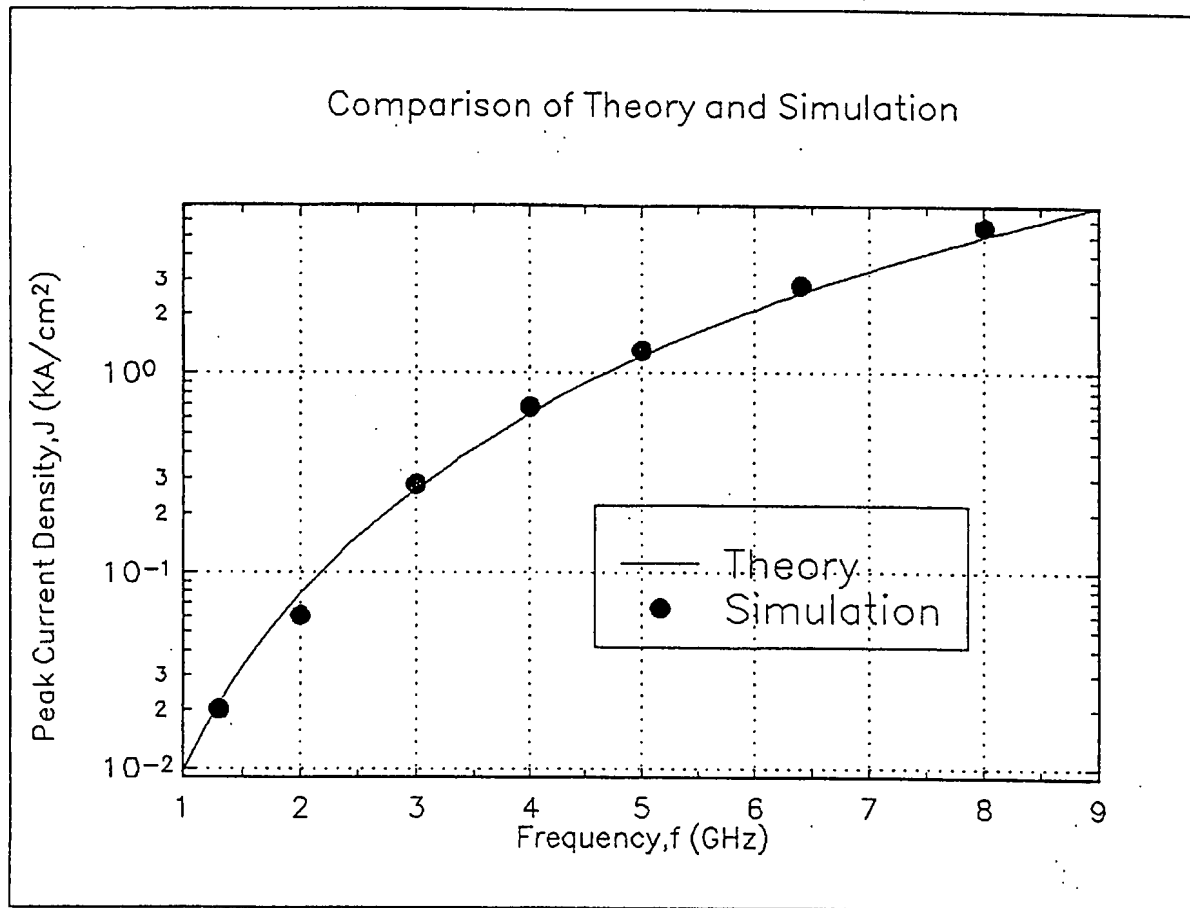


Figure 18: Comparison of peak current density in kA/cm^2 versus frequency for simulation and theory for a gap length of 0.5 cm and drive parameter $\alpha_0 = 0.453$.

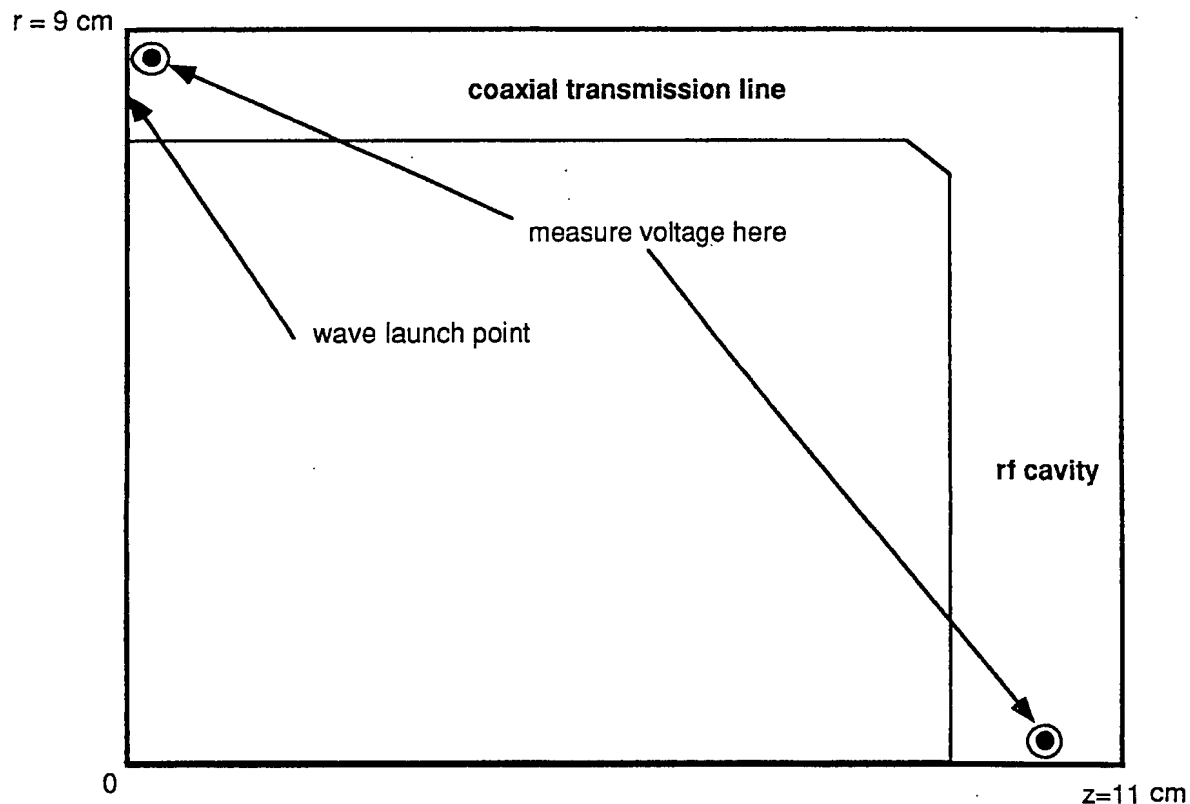


Figure 19: Side view of a cylindrically symmetric coaxial transmission line and cavity.
An rf wave is launched at the left end of the coaxial line.

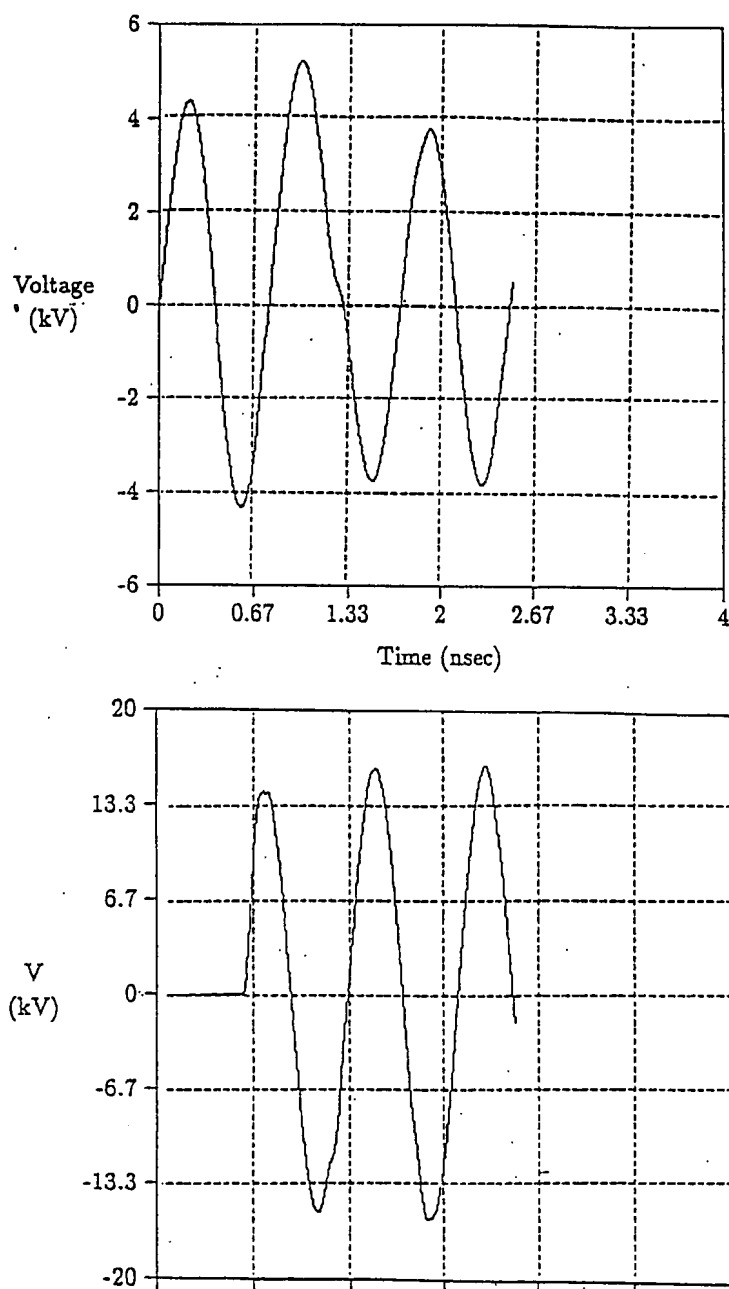


Figure 20: Resulting voltages for a TM_{010} cavity at 1.275 GHz (9 cm radius) with a one cm cavity gap and one cm coaxial gap. (top) voltage measured at entrance of coax, and (bottom) voltage measured at cavity center.

Electric Field vs Radius for an Ideal and a Coaxially Fed Cavity
 TM_{010} mode at 1.275 GHz, Cavity Gap=1 cm, Coaxial Gap = 1 cm

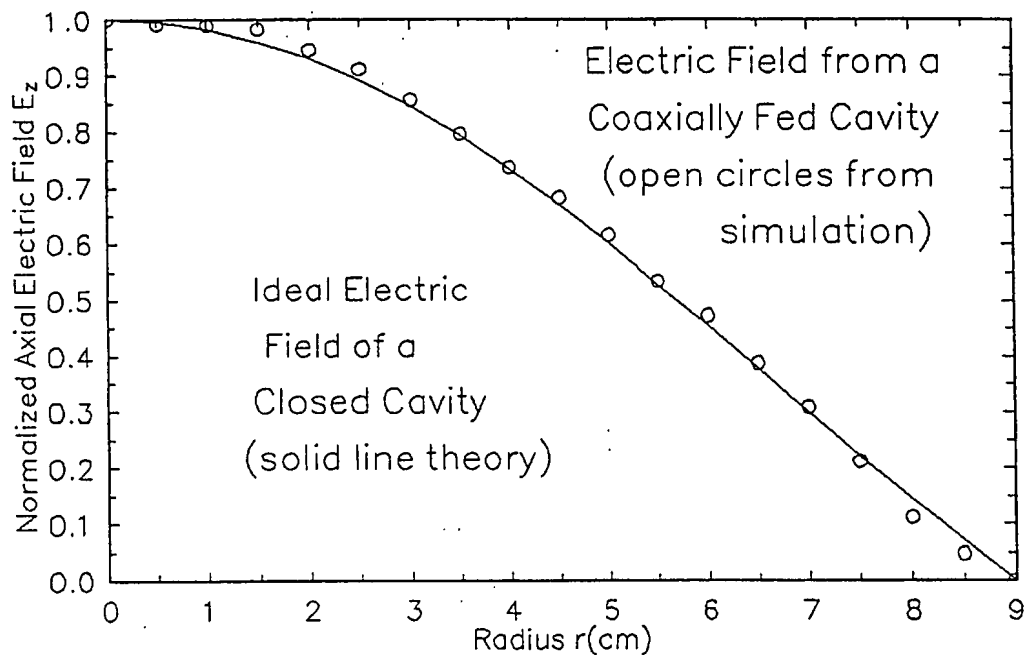


Figure 21: Electric field from a coaxially fed cavity (TM_{010} mode) showing simulation values (open circles) and theoretical curve for an ideal closed cavity.

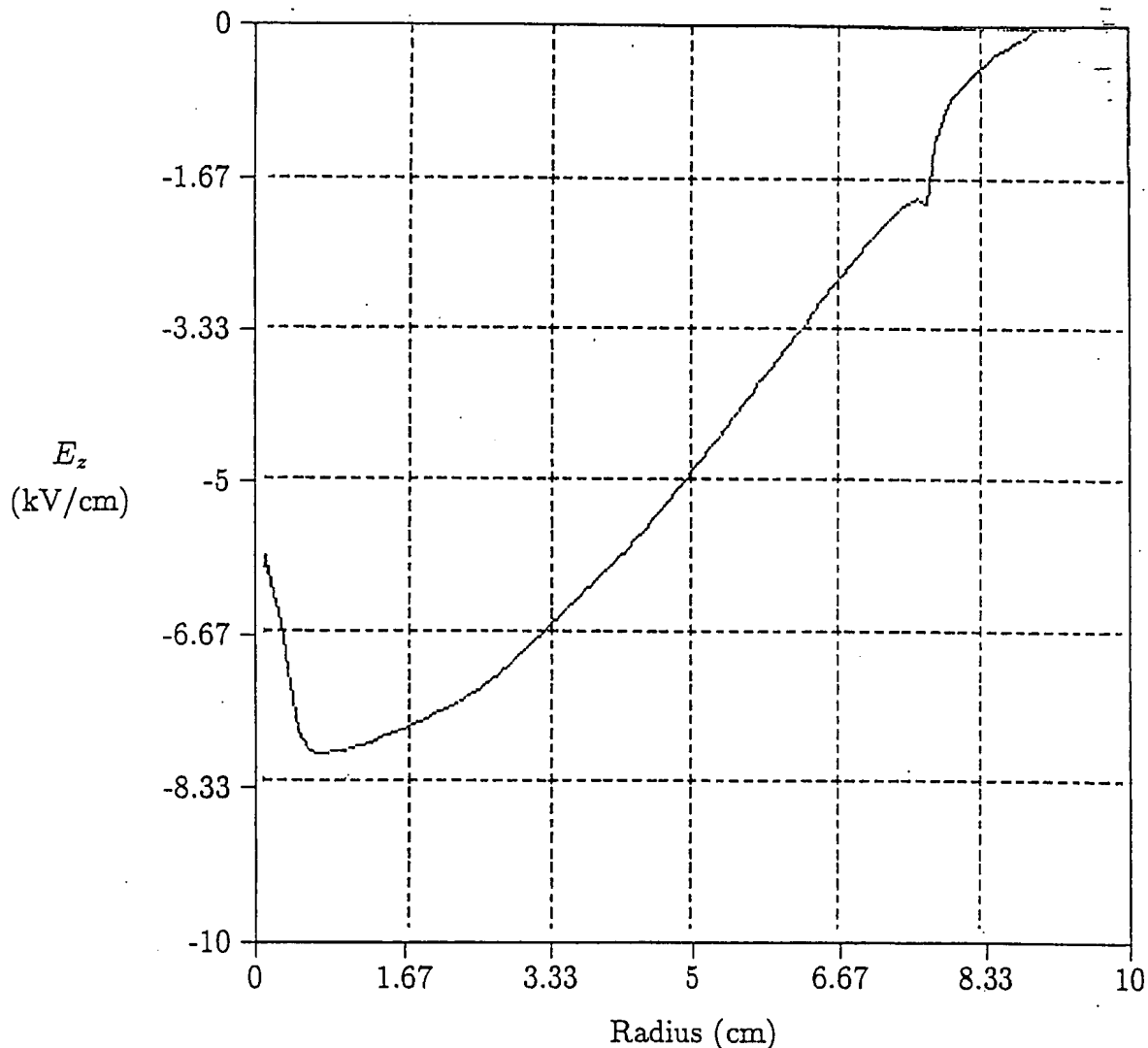


Figure 22: Axial electric field in cavity with a one cm diameter, $40 \text{ amp}/\text{cm}^2$, 25 ps long beam emitted into the cavity. The curve is inverted compared to the plot of Fig. 21. However, the depression at $R = 0 \text{ cm}$ due to space charge is clearly seen. Beam loading reduces the field by about 1/3.

Electric Field vs Radius for an Ideal and a Coaxially Fed Cavity
 TM_{020} mode at 1.275 GHz, Cavity Gap=1 cm, Coaxial Gap= 1 cm

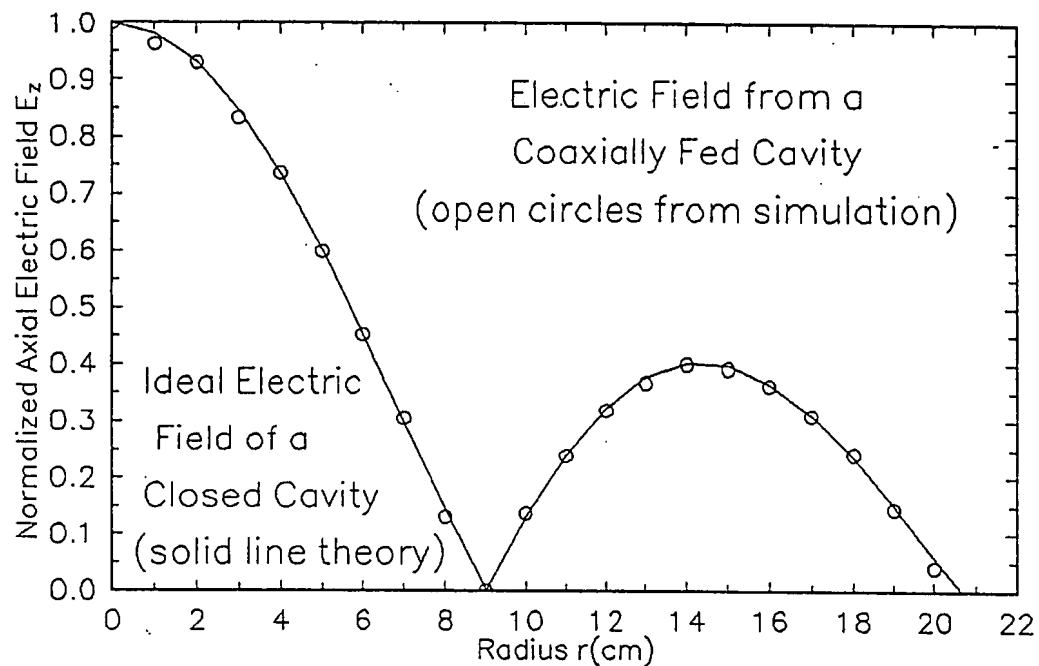


Figure 23: Electric field from a coaxially fed cavity (TM_{020} mode) showing simulation values (open circles) and theoretical curve for an ideal closed cavity.

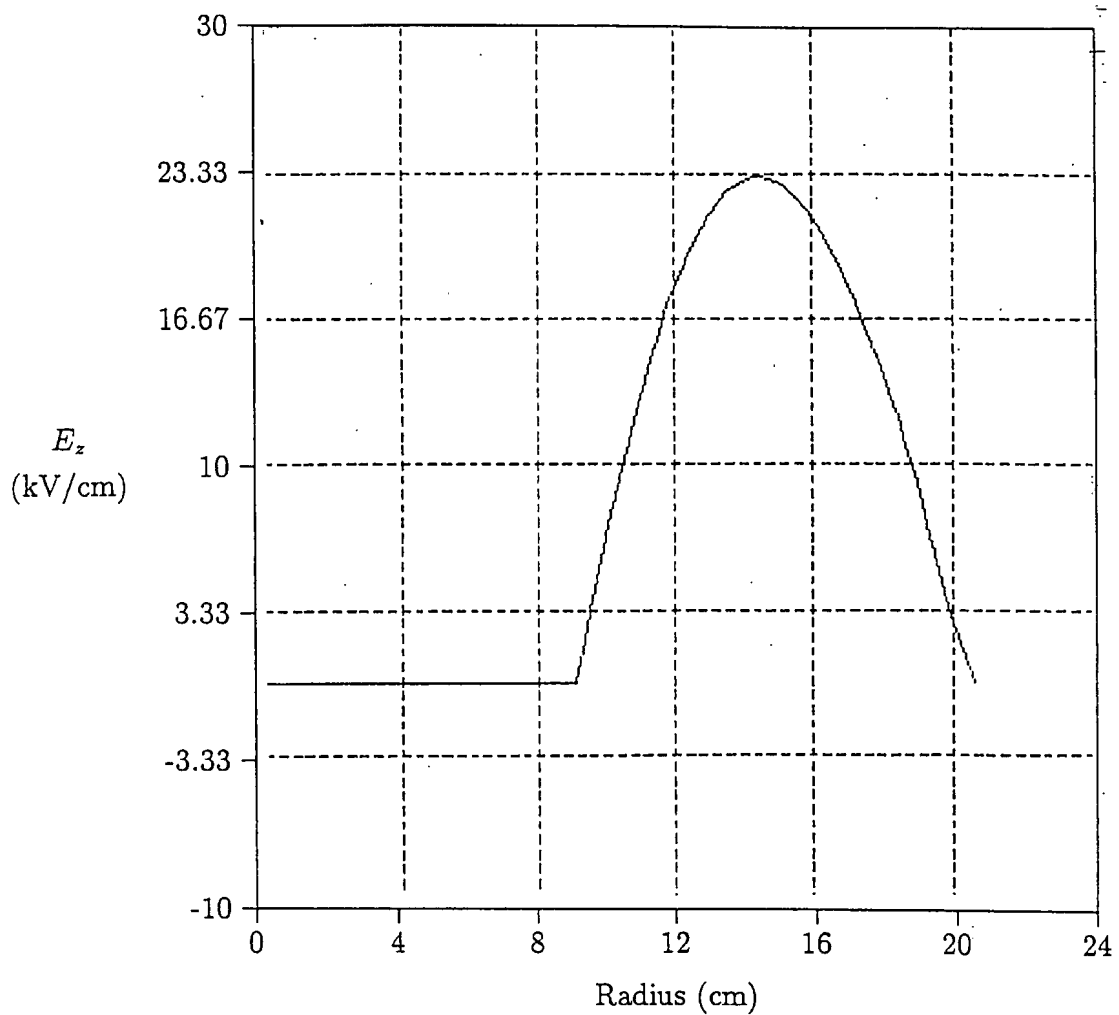


Figure 24: Axial electric field vs. radius from a coaxially fed cavity (TM₀₂₀ mode simulation) with inner conductor at first zero of the mode. The first peak has clearly been eliminated. Frequency 1.275 GHz and one cm gap.

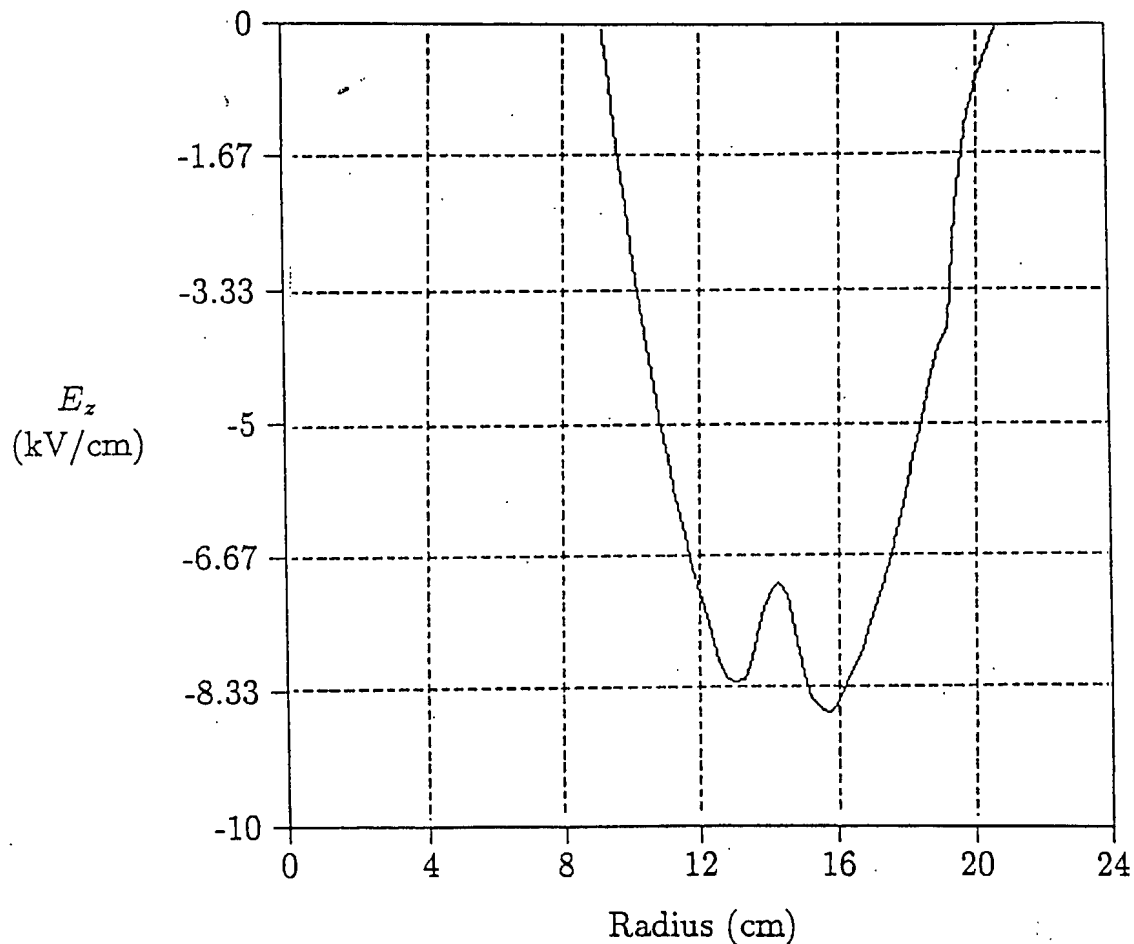


Figure 25: Axial electric field as a function of radius loaded down by a 40 amp/cm^2 , 25 ps pulse, and one cm diameter electron beam. The curve is inverted compared to the plot of Fig. 24. However, the depression at $R \approx 14 \text{ cm}$ due to space charge is clearly seen.

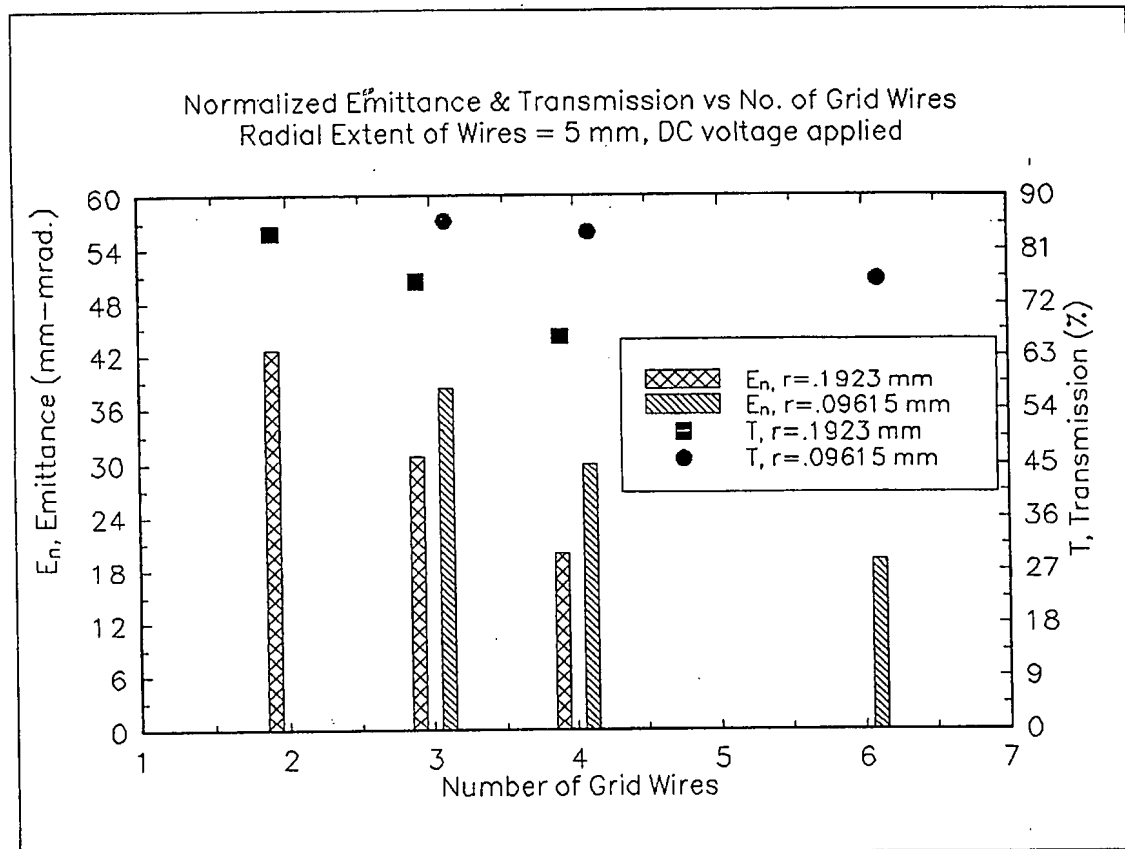


Figure 26: Normalized emittance and transmission versus number of grid wires with a dc voltage applied to the cavity.

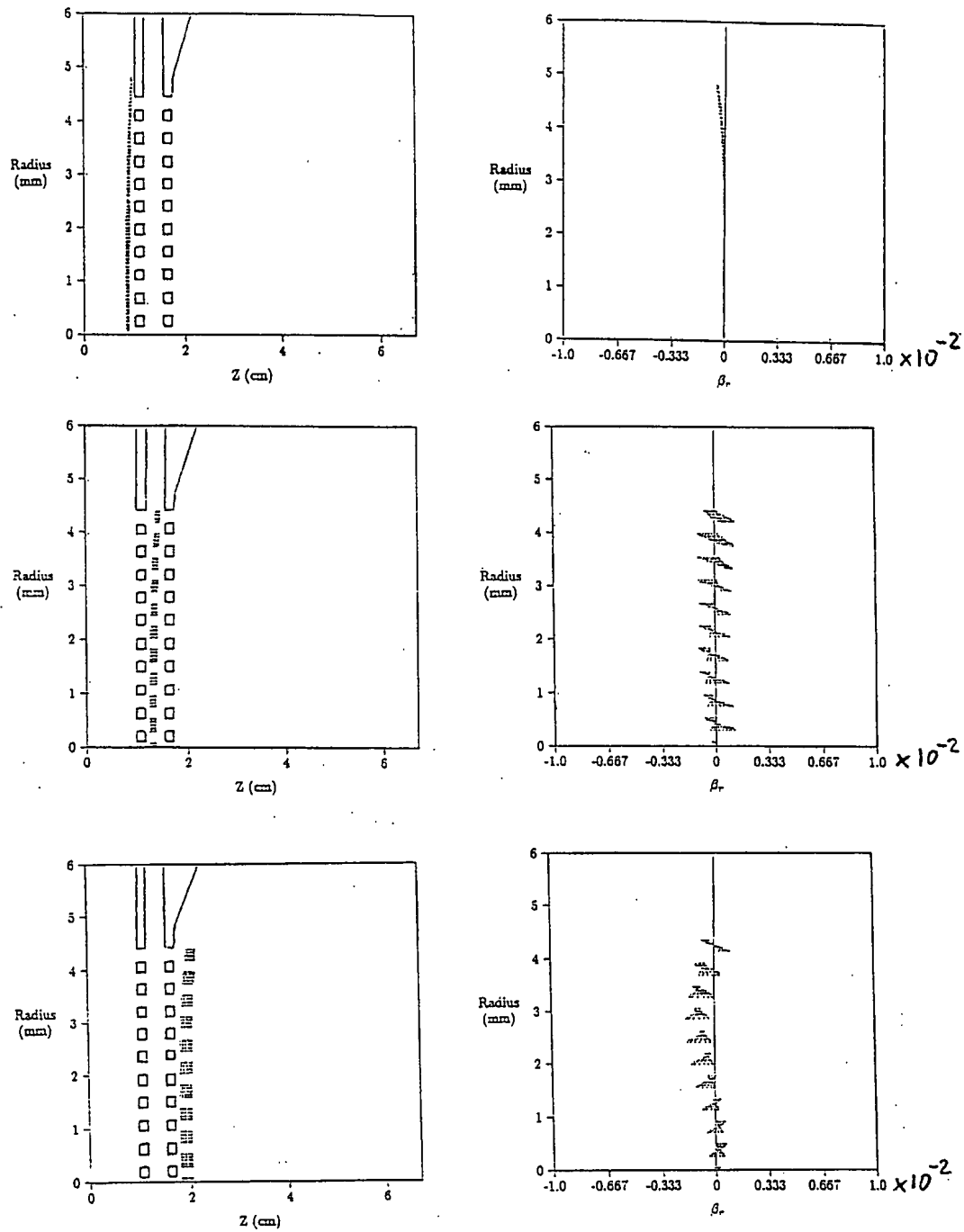


Figure 27: Configuration space and phase space for a solid beam from the simulations. This shows the emittance growth up to the first grid, from the first grid, and from the second grid.

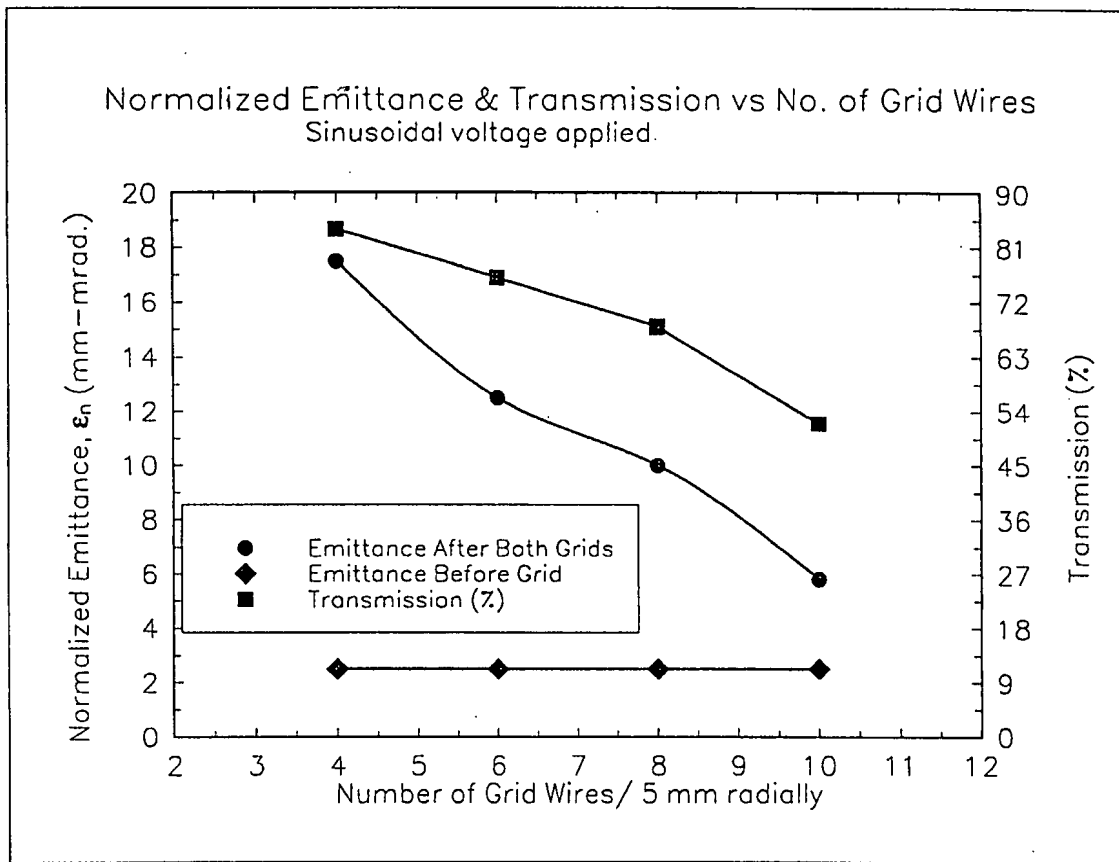


Figure 28: Normalized emittance and transmission versus number of grid wires with an ac voltage applied to the cavity. Grid wire radius is 0.09615 mm.

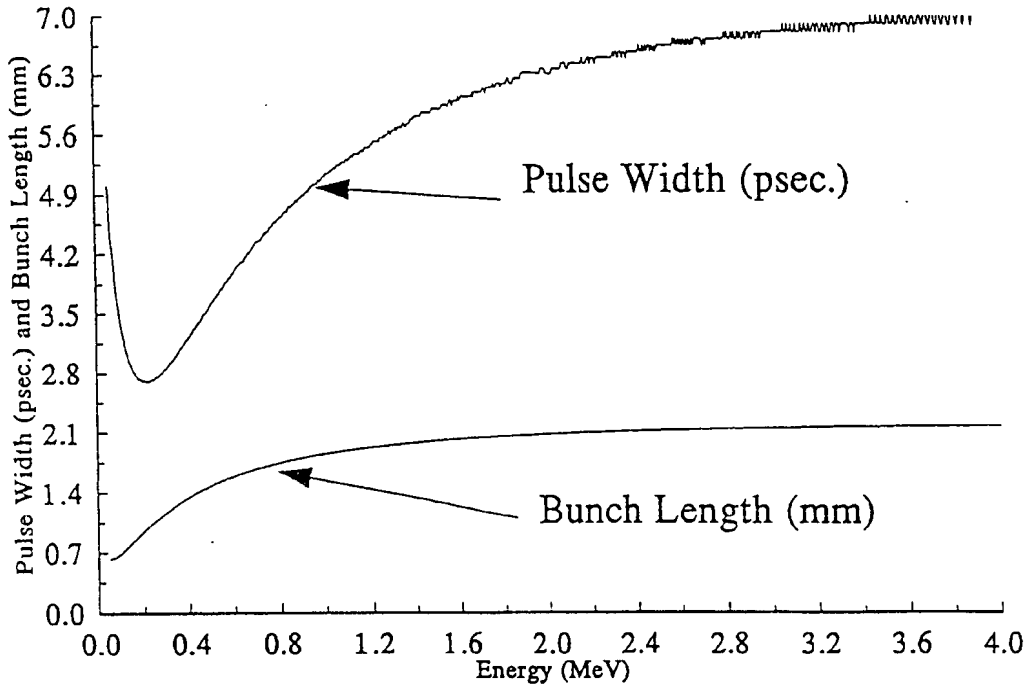


Figure 29: Expansion of micro-pulse from space charge during acceleration, neglecting energy spread. The acceleration field is 20 MV/m and the axial space charge electric field is 2.9 MV/m (corresponding to about 100 nC/cm³). The initial pulse width is 5 ps at an initial energy of 50 keV.

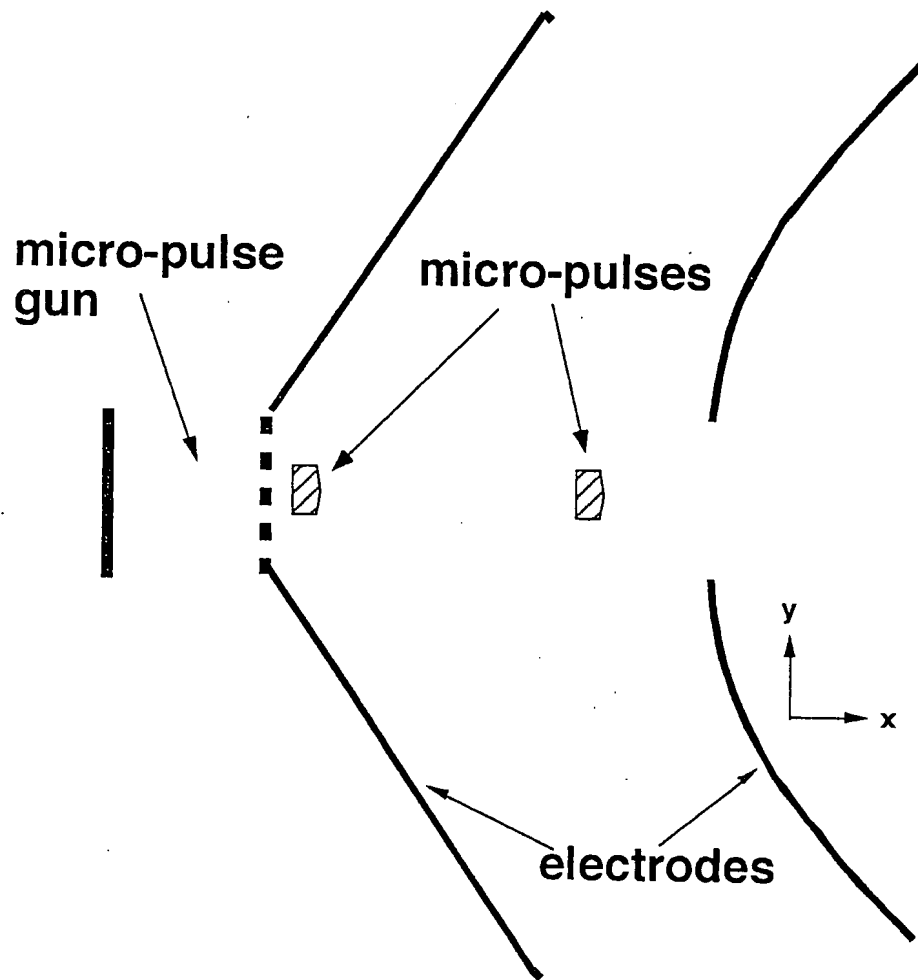


Figure 30: Schematic drawing of a set of electrode shapes for a high-power diode using the modified formulas to the usual Pierce shapes as discussed in the text.

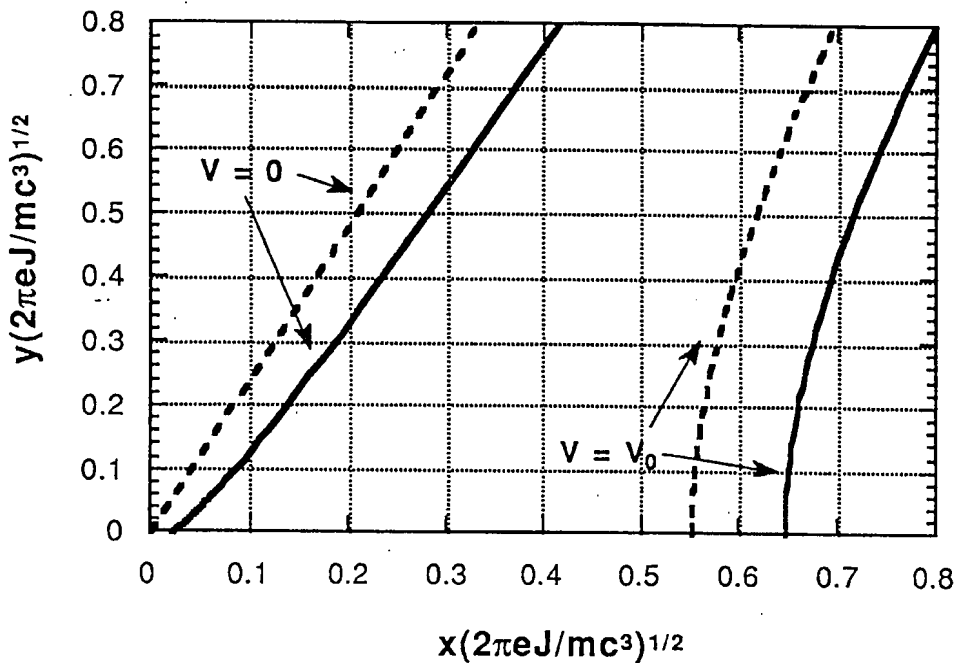


Figure 31: Plot of electrode shapes for a non-space-charge-limited 0.5 MeV diode. The modified shapes [solid lines] and the classical Pierce shapes [broken lines] are shown for comparison. The value of the electric field E_0 at the cathode is such that the quantity $\nu = 2$

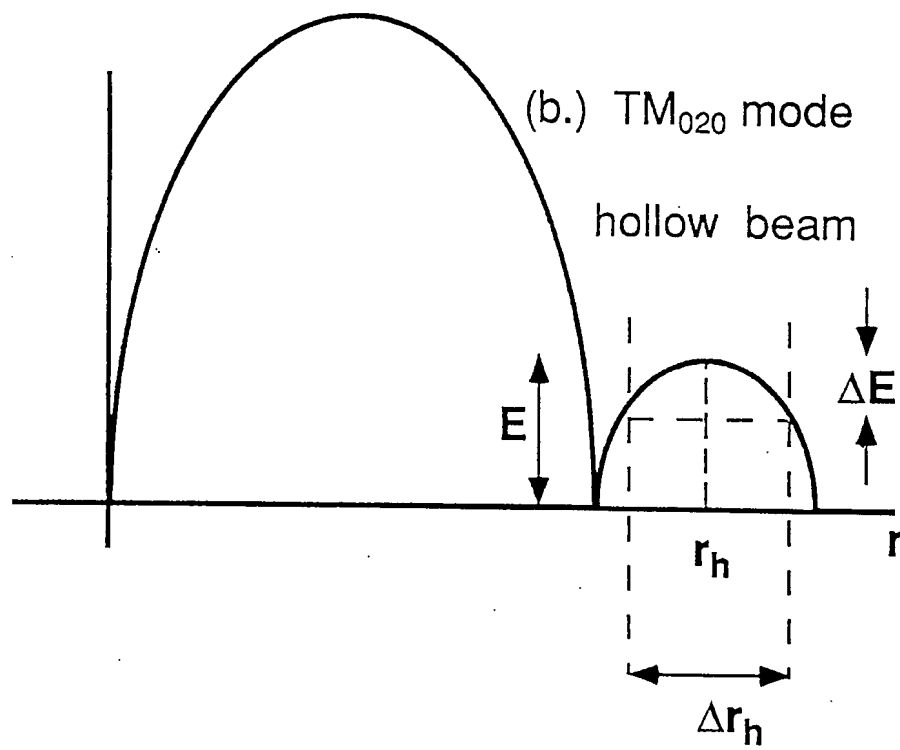
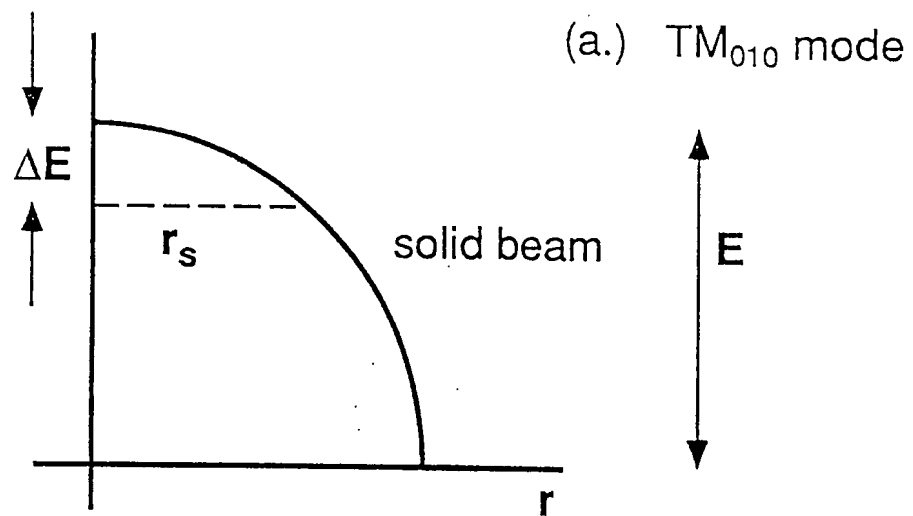


Figure 32: Schematic drawing of emission area and energy spread for a micropulse.

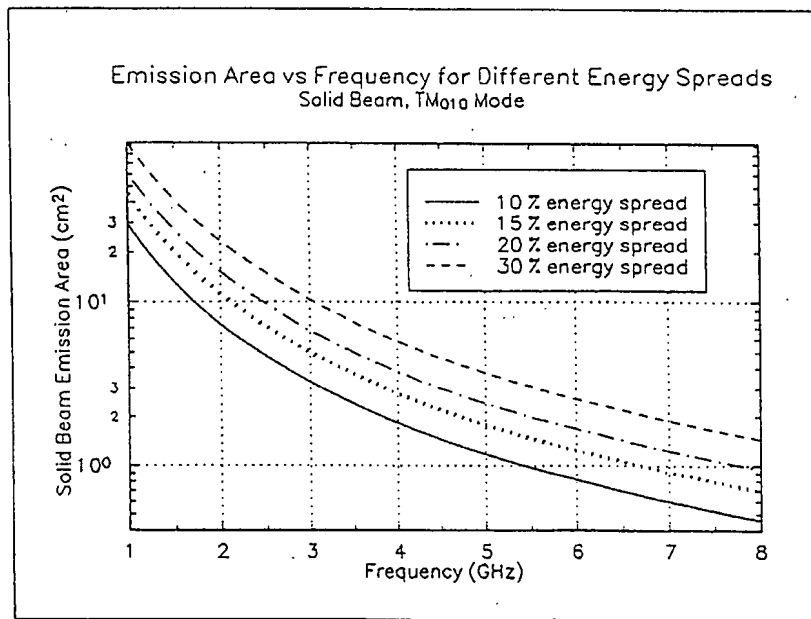
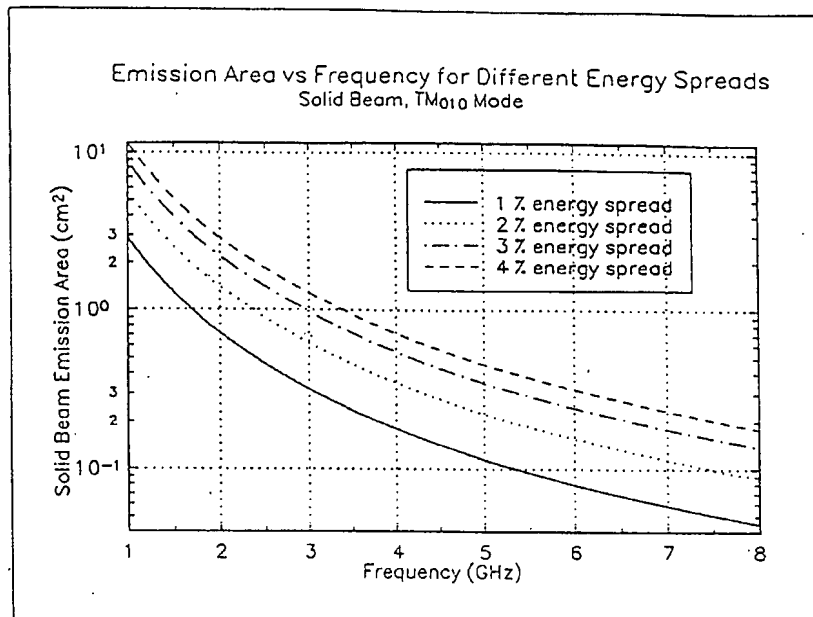


Figure 33: Emission area for a solid beam vs. frequency for different energy spreads (top)
1%-4% energy spread; (bottom) 10%-30% energy spread.

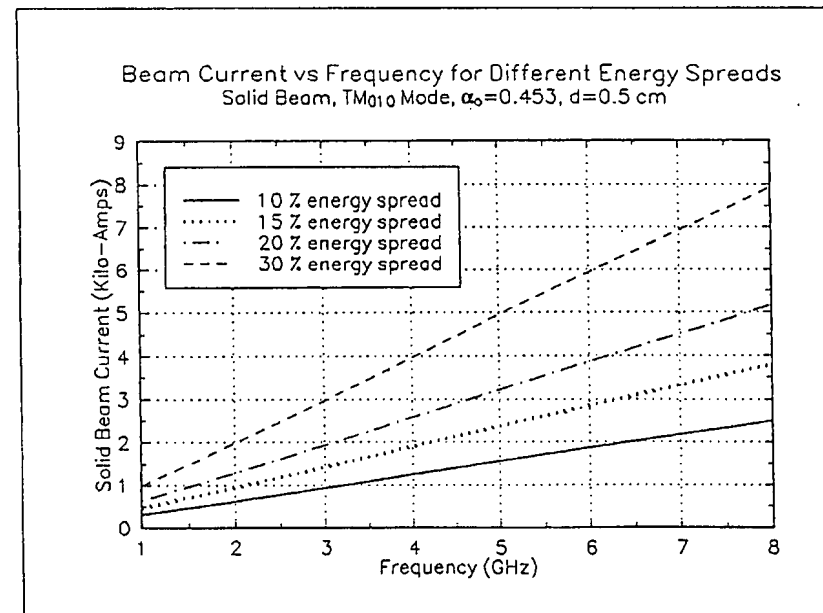
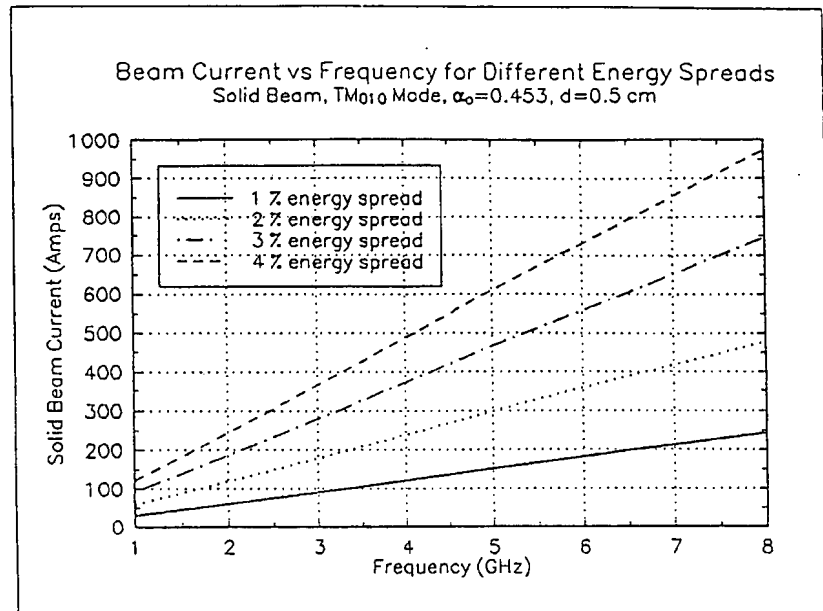


Figure 34: Beam current (solid beam) vs. frequency for different energy spreads and a gap of 0.5 cm.

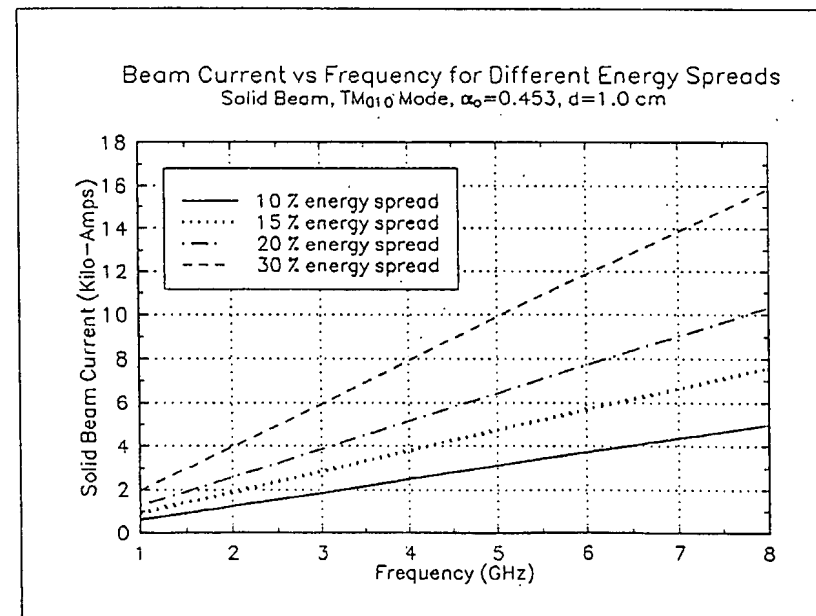
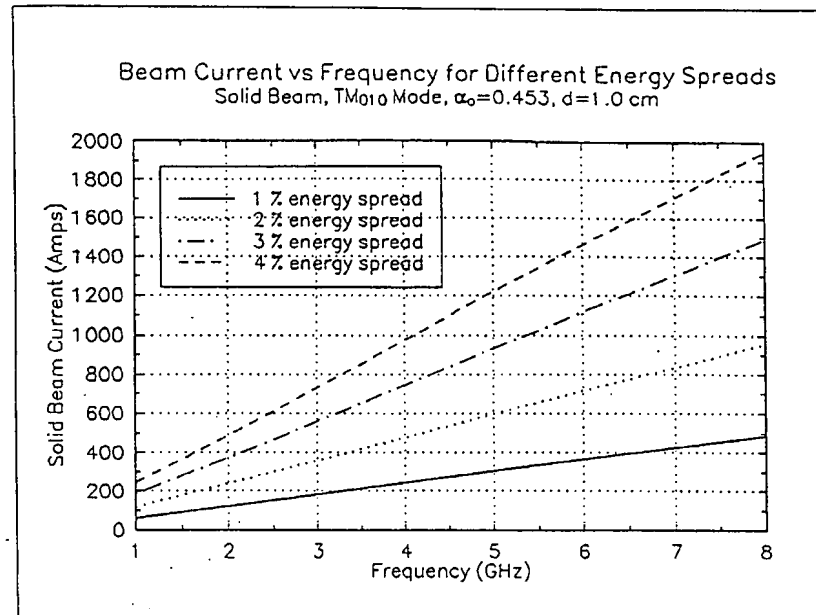


Figure 35: Beam current (solid beam) vs. frequency for different energy spreads and a gap of 1.0 cm.

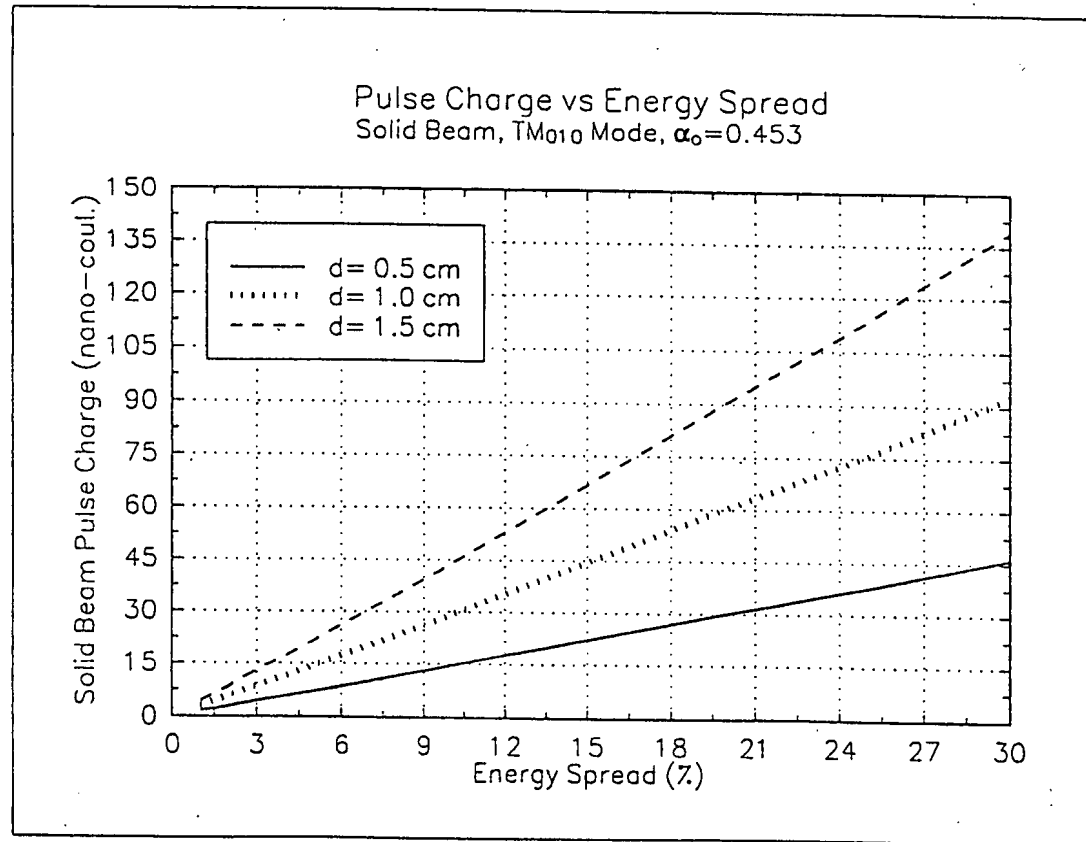


Figure 36: Charge per pulse for a solid beam vs. energy spread.

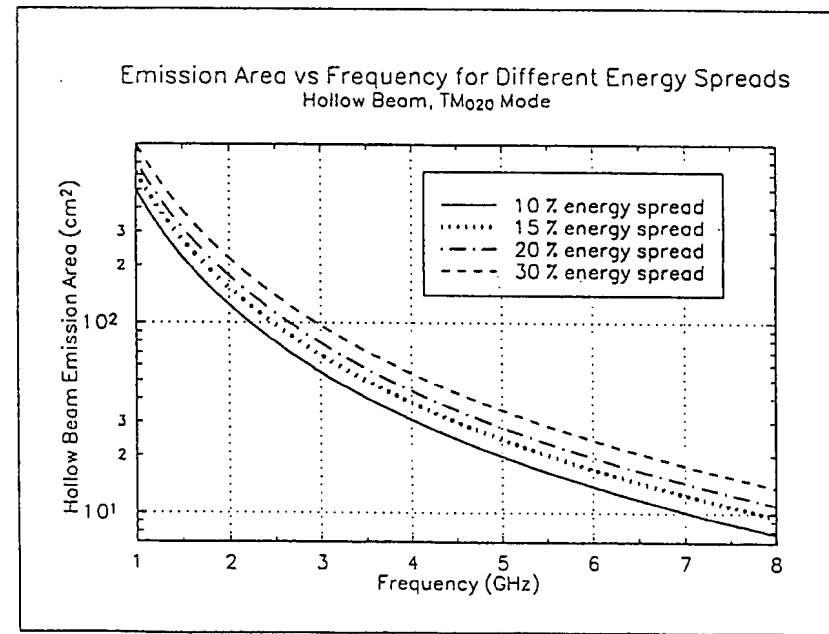
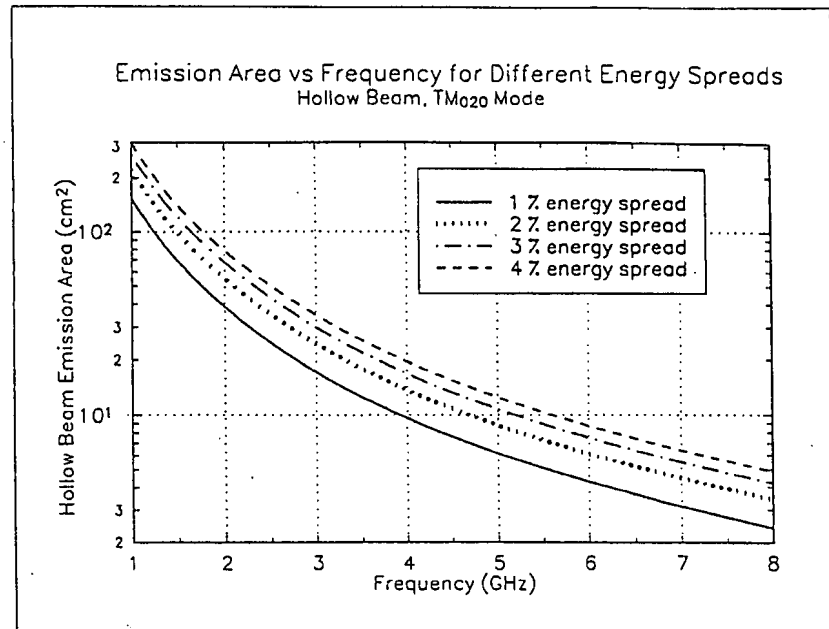


Figure 37: Emission area vs. frequency for different energy spreads. Hollow beam.

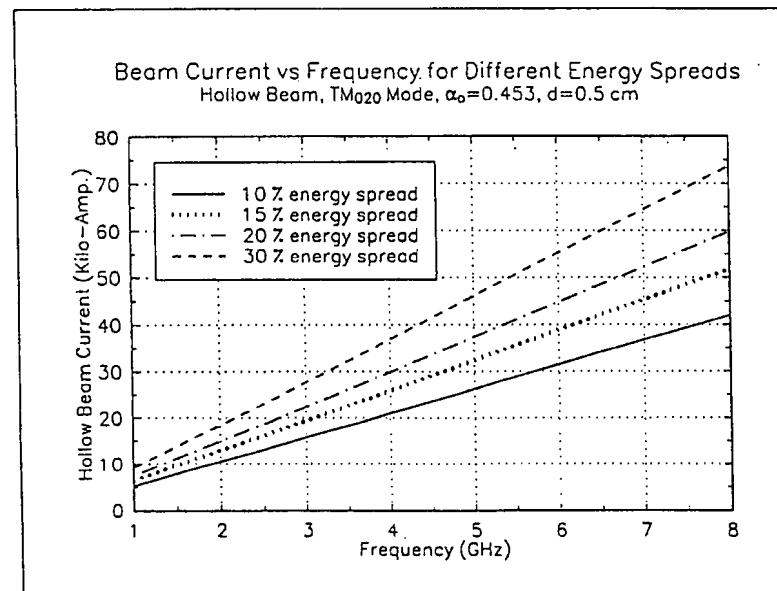
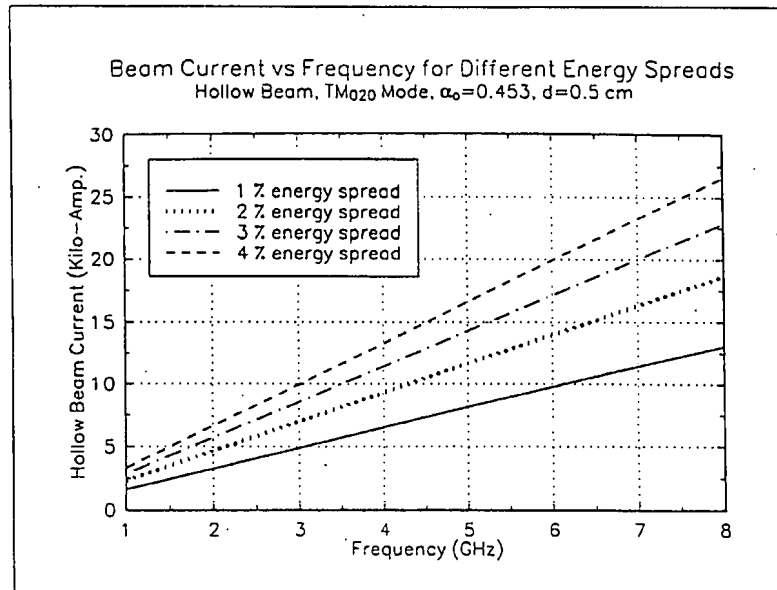


Figure 38: Beam current vs. frequency for different energy spreads. Hollow beam, and $d = 0.5$ cm.

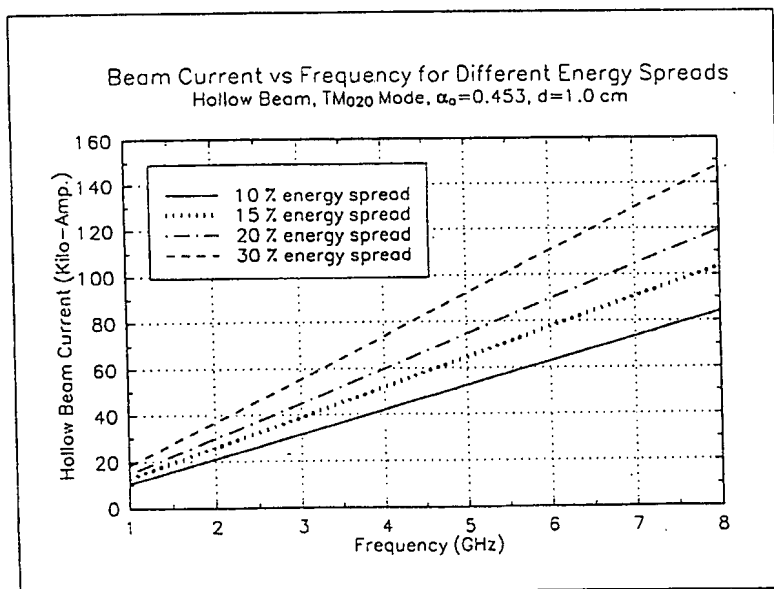
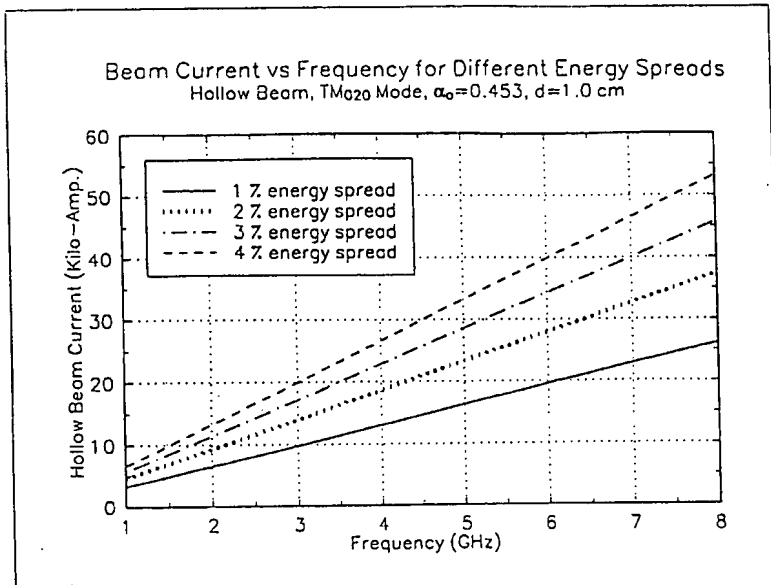


Figure 39: Beam current vs. frequency for different energy spreads. Hollow beam, and $d = 1.0$ cm.

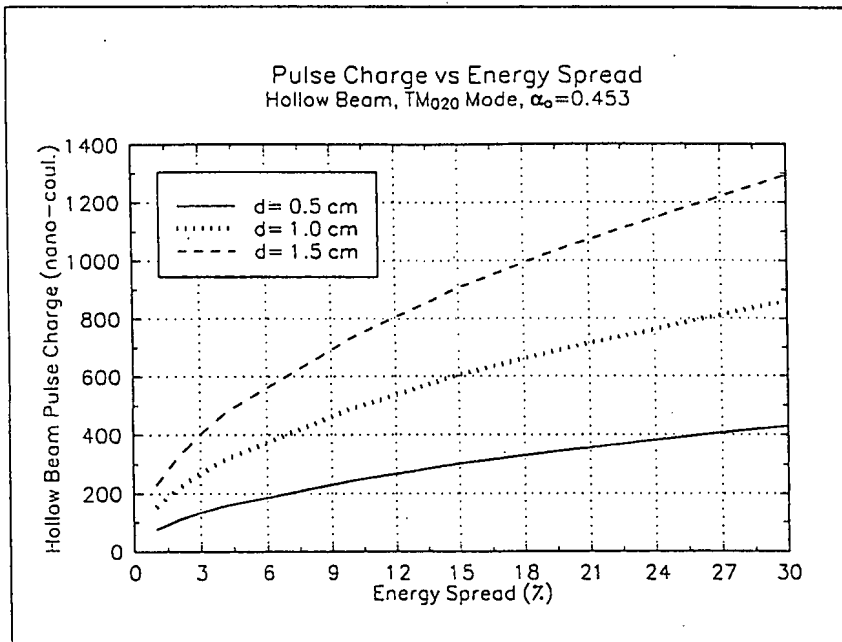


Figure 40: Pulse charge vs. energy spread for hollow beam.

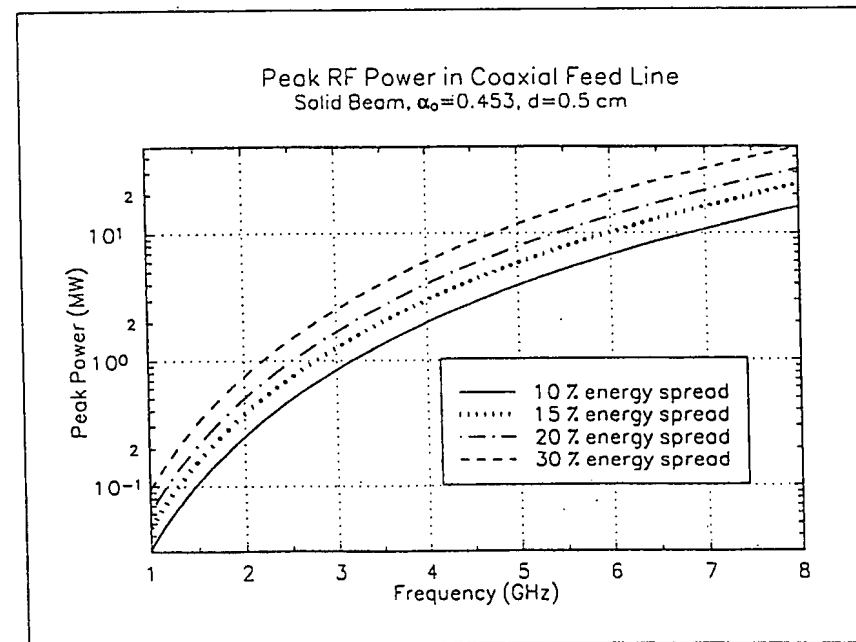
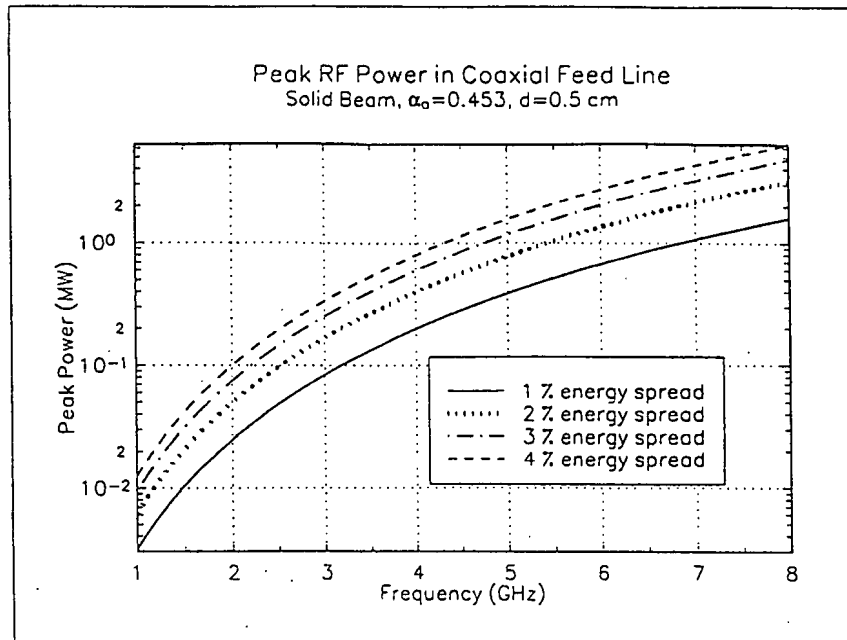


Figure 41: Peak rf power in coaxial feed line for a solid beam, $d = 0.5$ cm.

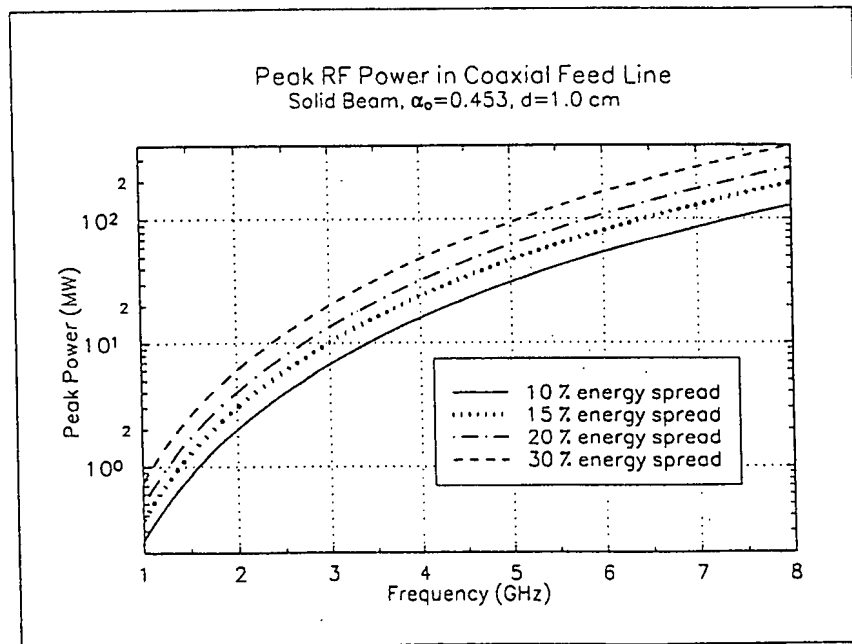
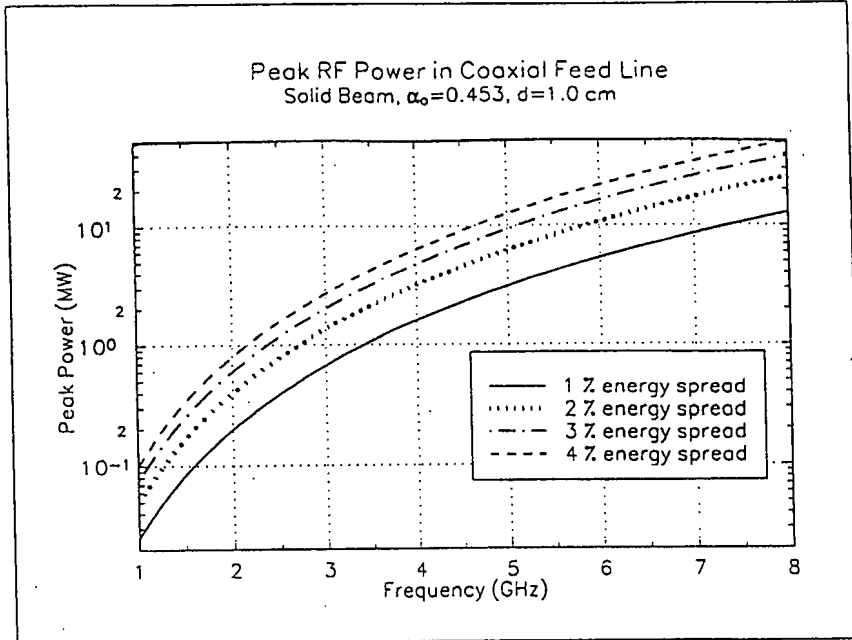


Figure 42: Peak rf power in coaxial feed line for a solid beam, $d = 1.0$ cm.

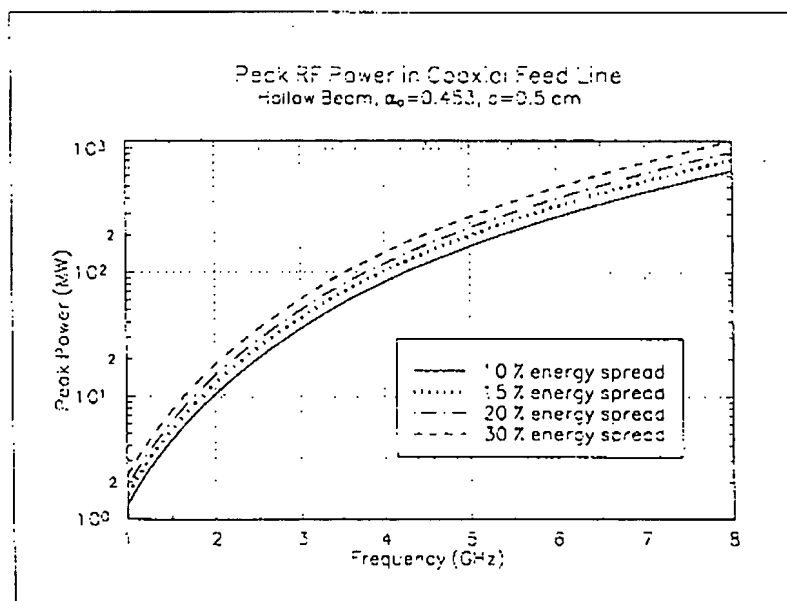
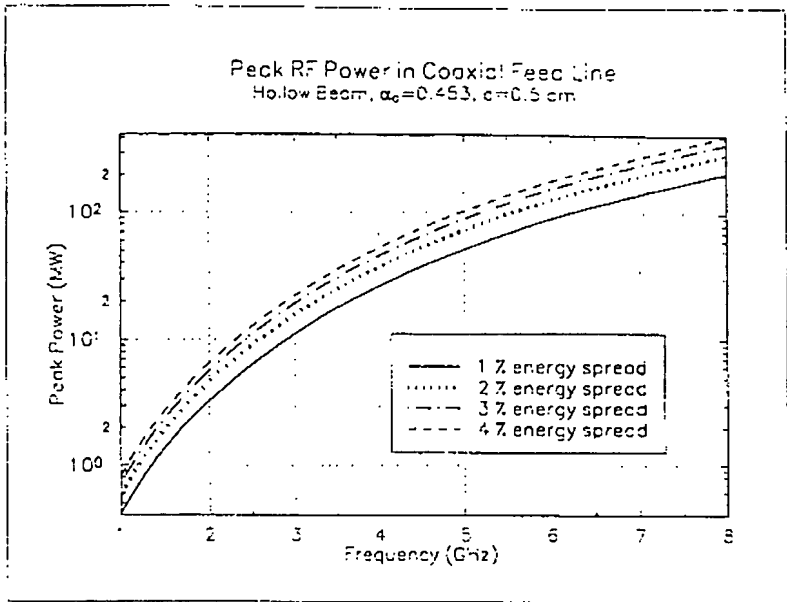


Figure 43: Peak rf power in coaxial feed line for a hollow beam, $d = 0.5$ cm.

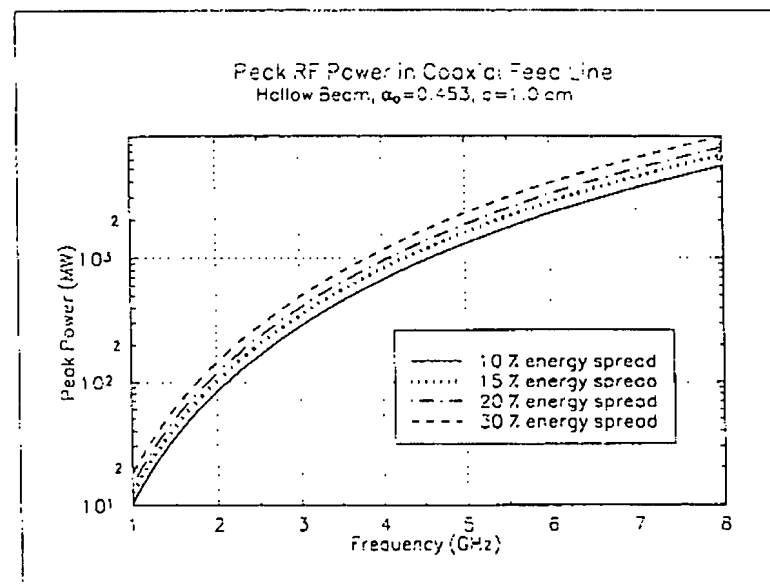
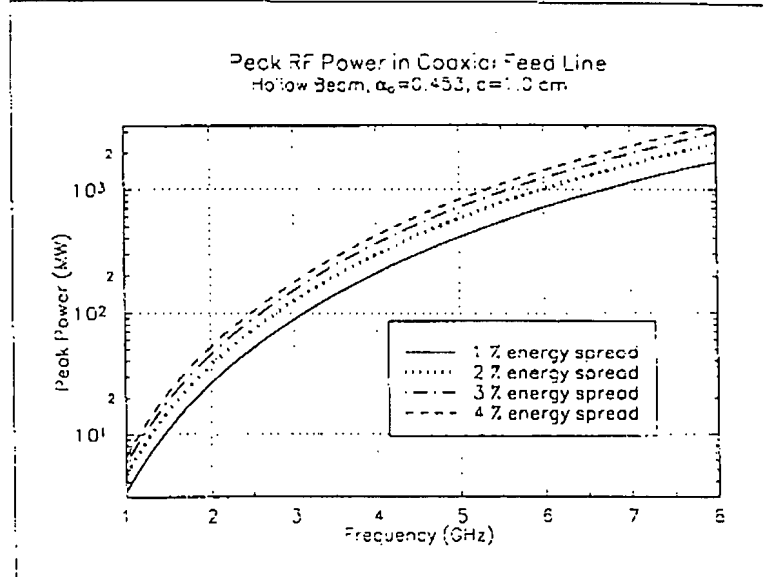


Figure 44: Peak rf power in coaxial feed line for a hollow beam, $d = 1.0$ cm.

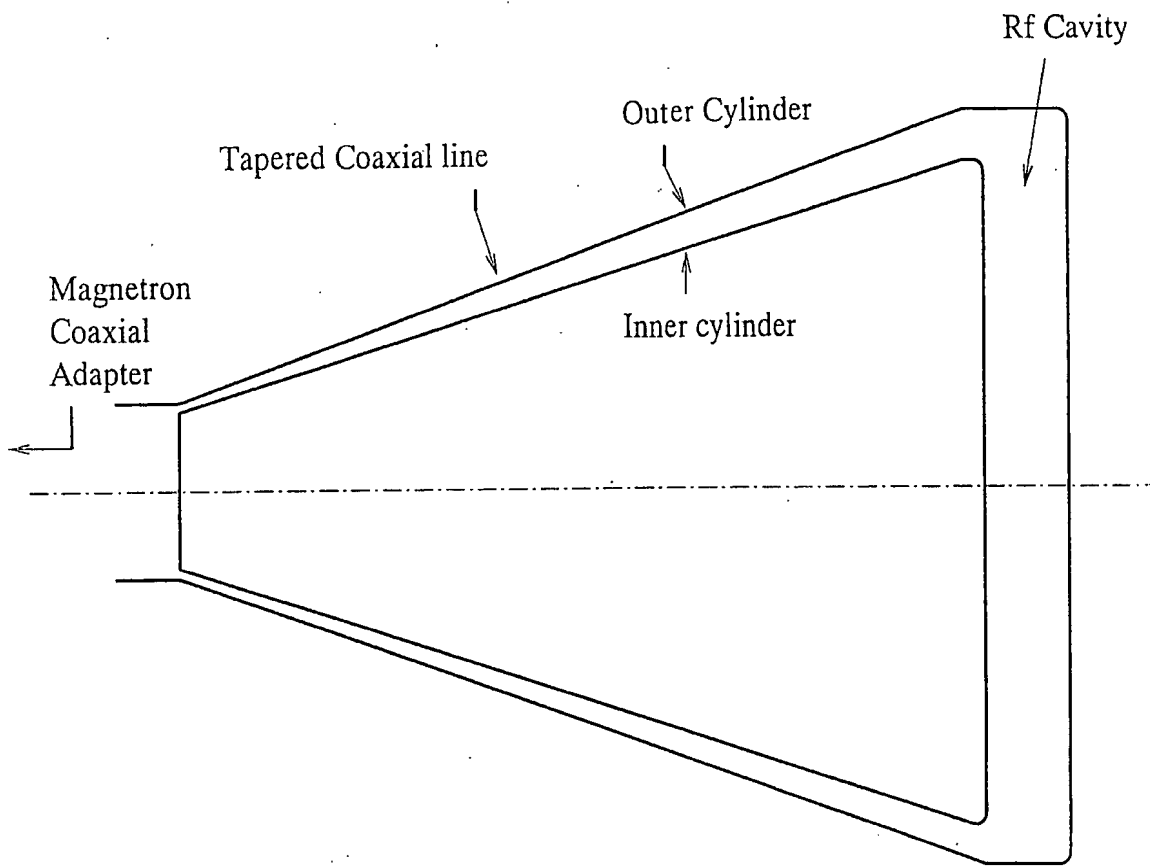


Figure 45: A magnetron feeding energy into the rf cavity. For simplicity a constant, low impedance, coaxial feed line is assumed. Voltage step-up occurs in the rf cavity.

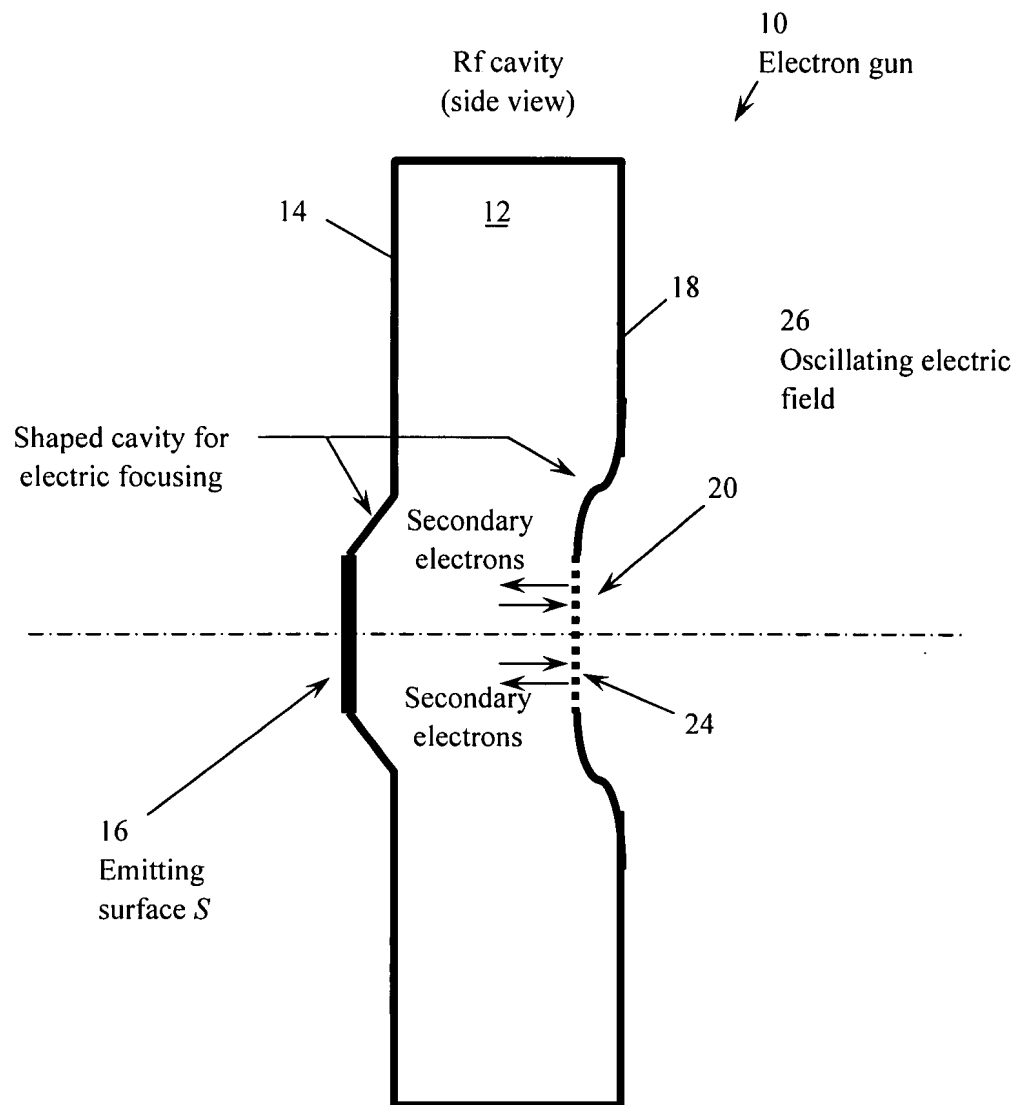


Figure 46: Schematic drawing of a possible design for electrostatic focusing in the MPG.